SHEIKH, T.M., ANWAR, M.P., MUTHOOSAMY, K., JAGANATHAN, J., CHAN, A. and MOHAMED, A.A. 2023. Graphene oxide's regenerative acidity and its effects on the hydration of type II Portland cement. *Construction and building materials* [online], 364, article 129933. Available from: https://doi.org/10.1016/j.conbuildmat.2022.129933

Graphene oxide's regenerative acidity and its effects on the hydration of type II Portland cement.

SHEIKH, T.M., ANWAR, M.P., MUTHOOSAMY, K., JAGANATHAN, J., CHAN, A. and MOHAMED, A.A.

2023

Supplementary materials are appended after the main text of this document.

Graphene oxide's regenerative acidity and its effects on the hydration of Type II Portland Cement

Taimur Mazhar Sheikh[1,4,*], Mohammed Parvez Anwar[1], Kasturi Muthoosamy[3,*], Jayaprakash Jaganathan[2], Andy Chan[1], Abdullahi Ali Mohamed[1]

University of Nottingham Malaysia, Jalan Broga, Semenyih 43500, Selangor Darul Ehsan, Malaysia

Abstract

Incorporation of Graphene oxides (GO) has been found to considerably improve the hydration process, strength and durability of Portland cement. However the exact nature of its chemical interactions with the cement are unclear. Thus, GO of varying amounts of hydroxyl groups were synthesized to investigate their effects on the hydration of an environmentally friendly Type II Portland Cement. XPS, Raman, and FTIR analysis verified the functional group differences between the GO types, and SEM and AFM analyses visually confirmed the existence of a hydronium layer coating the high-hydroxyl GO (HGO). The hydronium layer neutralizes small base additions as measured through titration, and regenerates via protonation of resulting water by HGO's hydroxyl groups, which was confirmed via zeta potential analysis. When added in cement, HGO shows accelerated and greater early-age cement hydration, measured via heat of hydration and XRD tests. Finer microstructural density of HGO-cement was also observed using BET and microCT analysis. It is hypothesized that the hydronium layer 'caps' the calcium-silicate-hydrate (C-S-H) molecules at early stage hydration, allowing movement which forms a highly inter-connected cement matrix. Conversely, low-hydroxyl GO (XGO) cement 'locks' C-S-H on the GO sheet, preventing the C-S-H from propagating in the cement microstructure. This hypothesis was supported by measuring the changes in C-S-H Si-O bond wavelengths during hydration. These results confirm molecular simulations between C-S-H and GO particles in literature. Lastly, HGO-concrete showed significantly improved workability (>40%), 28-day compressive strength (29%), and 28-day flexural strength (24%) with respect to control. Conversely, XGO-concrete showed reduced workabiltiy (-40%), and smaller 28-day strength improvements (compressive by 5%, and flexural by 8%). This research leads to new understandings of how GO may improve the strength, workability, and durability of concrete, with potentially less overall cement consumption and superplasticizer use.

---

[*] Corresponding authors

Email addresses: `taimur.sheikh@wecuw.edu.pk` (Taimur Mazhar Sheikh), `kasturi.muthoosamy@nottingham.edu.my` (Kasturi Muthoosamy)

[1] Department of Civil Engineering, Faculty of Science and Engineering, University of Nottingham Malaysia, Jalan Broga, Semenyih 43500, Selangor Darul Ehsan, Malaysia

[2] School of Civil Engineering, Vellore Institute of Technology, Vellore Campus, Tiruvalam Rd, Katpadi, Vellore, Tamil Nadu 632014, India

[3] Nanotechnology Research Group, Centre of Nanotechnology and Advanced Materials, University of Nottingham Malaysia, Jalan Broga, Semenyih 43500, Selangor Darul Ehsan, Malaysia

[4] Department of Civil Engineering, Wah Engineering College, University of Wah, Wah Cantt, 47040, Pakistan

Keywords: , nanomaterials, graphene oxide, concrete, cement, microCT, functionalized

---

1. Introduction

Portland Cement (PC) is widely used in the concrete construction industry due to its cost-effectiveness, versatility and ease of application. It's production, however, is not environmentally sustainable, emitting approximately 8% of the world's carbon dioxide (CO_2) [1]. PC reacts with water in a process called hydration, forming a binding agent that holds aggregates together in concrete (curing), resulting in high compressive strength and good durability. However, not all PC in the structure reacts with water, with certain high-cement concretes only using 30-50% of the total cement during the 28-day curing process, a considerable waste [2]. Thus, cement wastage can be reduced by maximizing its total hydration potential in structures, and minute additions of graphene oxide (GO) nanoparticles have shown to improve the hydrated cement microstructure significantly [3]. GO is an oxidized form of graphene, which is a 2D sheet structure of carbon atoms typically arranged in a hexagonal, honeycombed pattern. Graphene sheets with added oxygen atoms in hydroxyl (C-OH), epoxy (C-O-C), carbonyl (C=O), and carboxyl (O=C-OH) formations result in GO. These added functional groups make GO polar and easily dispersible in water. As cement requires access to water molecules for hydration, GO's polarity concentrates a large amount of water molecules in its proximity, providing 'seeding' points for cement particles to latch on. This allows quicker and higher overall hydration, and therefore produces a cement strengthening effect with denser microstructure [4, 5, 6]. Additionally, GO sheets can interlink in alkaline solutions, connected by free-floating divalent calcium (Ca^{2+}) ions in aqueous solutions [7]. Free-floating Ca^{2+} is also found in cement matrix during the curing process, and PC is considerably weak under tensile and flexural loading, hence interlinking can possibly provide higher flexural resistance to cement [8, 9]. Despite the known advantages of GO-cement, a key issue of GO incorporation is the unpredictability of its strength and durability improvements in cement [10], and this research aims to identify the chemical interactions between the GO and cement during hydration.

To understand how GO is improving cement hydration, its role as a 'seeding' point should be addressed. GO sheets have typically high aspect ratios, with narrow sheet thickness (approximately 1 nm) and varying lengths from 500 nm to several μm [11]. The hydroxyl and epoxy groups of GO mainly exist on the surface of the sheets, while carboxyl groups are found at the edges. That is because carboxyl groups require 3 covalent bonds from each carbon atom, which is only possible at the terminal edges of the GO sheets. Hence, it can be inferred that the hydroxyl and epoxy groups are primarily responsible for attracting the polar water molecules around GO. Indeed, molecular simulations indicate GO sheets are easily dispersed by hydrogen bond networks between GO's surface functional groups and water molecules [12]. First principle simulations also show active proton (H^+) transfer between the GO hydroxyl groups and surrounding water molecules [13], which leads to an interesting aspect of GO: its acidity in aqueous solutions. GO solutions are shown to have pH between 2 and 3, lower than saturated carboxylic acids [14]. As GO typically has few edge carboxyl groups, the acidity must be from the proton transfer between hydroxyl groups and water molecules. Moreover, GO tends to undergo decarboxylation in alkaline conditions, which could be due to the vinylogous activity of the GO sheet and hydroxyl groups [15]. A dynamic interchange of H+ is found between GO's hydroxyl groups and water, leading to an equilibrium of H2O and protonated hydronium (H_3O^+) surrounding the GO sheet [14]. The opposite charges of deprotonated hydroxyl groups (C-O^-) and H_3O^+ result in a dynamic hydronium layer being electrostatically attracted to GO, which has possibly been observed as oxidative debris in earlier research [16].

It is proposed that this hydronium layer is the primary seeder for C-S-H nucleation and growth during cement hydration, as it is the first point of contact for the dissociating cement particles. GO is exposed to cement only when the layer is successfully deprotonated, which is an expected outcome due to the alkaline by-products of the hydration reaction. As the hydronium layer originates from GO hydroxyl groups' reaction with water molecules, it follows that the amount of hydroxyl group on GO's surface can affect its subsequent contribution to cement hydration. Hence, using Chen et al's [17] findings, three GO with different amounts of hydroxyl groups were synthesized: a high-hydroxyl GO (HGO), a low-hydroxyl, partly reduced GO (XGO), and GO synthesized using Marcano's [18] modified Hummer's method (OGO), which has a moderate amount of hydroxyl groups. Their acidities are measured, and their effects on the hydration and microstructural development of cement, and the strength and workability of concrete is investigated.

2. Methodology

2.1. Synthesis of GO

For ordinary graphene oxide (OGO), as per Marcano et al. [18] 13.4 mL 85% phosphoric acid (H_3PO_4, Chemiz) was added to 120 mL of 95-97% concentrated sulphuric acid (H_2SO_4, Fulltime) (9:1 ratio) and the mixture was allowed to cool to 20 °C. 1 g of graphite powder (<20 μm Sigma-Aldrich) was added and the mixture was stirred at 300 rpm for 10 minutes to allow intercalation. After 10 minutes, 6 g of solid potassium permanganate ($KMnO_4$, Chemiz, 6 wt. equivalent) was added slowly to the intercalated graphite mix over a period of 5 minutes. During this period, the mix warmed to approximately 35 °C, after which it was kept under constant stirring in a fume hood at a room temperature of 20 °C for 120 hours. The temperature was not increased as per Chen et al. findings [17] where keeping a low temperature typically increases the yield of GO. After 120 hours, 30% hydrogen peroxide (H_2O_2, R&M Chemicals) was added drop-wise alternating with 135 mL of ice cubes to keep the temperature below 60 °C. The quantity of H_2O_2 varied for each GO type: OGO required 5 mL of H_2O_2 until the colour turned pale yellow and temperature rise subsided, indicating oxidation reaction termination. The initial filtrate was brown in colour and darkened with successive washing. For high-hydroxyl graphene oxide (HGO), the oxidative treatment is similar to OGO, except after the intercalation period (10 minutes of stirring of graphite in 9:1 H_2SO_4:H_3PO_4 acid mix), where 10 mL of distilled water is added slowly to the mix as per Chen et al. [17], followed by $KMnO_4$ (6 wt. equivalent) and the remaining procedure is similar to OGO. For termination, it is found only 3.5 mL of H_2O_2 was required for the mix to turn pale yellow, and subsequent addition of H_2O_2 resulted in no colour change or rise in temperature. The decontamination and sonication of HGO was followed similar to OGO. Noteworthy, HGO was lighter brown in colour than OGO, however the solution darkened over a period 1-2 weeks, as did all the GO variants. For low-hydroxyl graphene oxide (XGO), the intercalation and oxidation procedures are similar to OGO, however after 120 hours and prior to termination, 100 ml of water was slowly added and the GO mix was heated to 95 °C and maintained at that temperature for 15 minutes [17]. Visually, the mix changed colour from deep purple to dark mahogany brown, with pale yellow frothing was observed during the heat treatment. After 15 minutes, the mix was allowed to cool and any addition of H_2O_2 did not change its colour or cause temperature rise. All three GO solutions were allowed to cool to room temperature and decontamination process was initiated, first by centrifuging each solution at 7500 rpm for 30 minutes, after which the supernatant was discarded. The filtrate was washed with 1 M HCl and centrifuged at 7500 rpm for 30 minutes (eppendorf 5810R), after which the filtrate was extracted and subjected to 2 more rounds of washing and centrifugation with 1 M HCl. After 3 repeats, the filtrate was washed with distilled water and centrifuged (7500 rpm) for 30 minutes, and this step was repeated for 7 times. After final centrifugation, the filtrate was added to 100 mL distilled water and stirred manually until all visible particles were mixed evenly. It was then placed in an ultrasonicating bath and sonicated for 20 minutes (Elma Transsonic 35 kHz, 40% intensity). Finally, distilled water was added until total volume reached 500 mL.

2.2. Analytical tests

For FTIR and SEM, all GO samples were heated to 65 °C for 48 hours prior to testing (oven-dried samples). Moreover, separate GO samples were freeze dried for 72 hours and stored in a desiccator with silica gel until FTIR/SEM was conducted. FTIR (Perkin Elmer Frontier) analysis was carried out with 10 scans from 4000 to 400 cm^{-1} wavelengths. The spectra was averaged and base corrected using the Perkin Elmer Spectrum 10 software. FEI Quanta 200 3D Dual Beam FIB-SEM machine was used for imaging of GO and GO-cement samples. The Quantera II, ULVAC-PHI XPS was used with an Al Kα X ray source (25 W, voltage source 15 kV) with beam size 100 μm at tilt angle of 45° for far and near XPS spectra scan (C1s and O1s). Pass energy was kept at 112 eV, with a dwell time of 20 ms per step. The 633 nm wavelength was used to acquire the D and G peaks from Raman testing. 1 mg/mL GO solutions were spin-coated on glass cover-slips using a KISKO Specialty Coating System 6800 machine (3000 rpm for 60 seconds) for sheet size measurements via SEM and AFM analysis (Hitachi AFM5100N, using Dynamic Force Microscopy).

50 mL of 1.5 mg/mL concentrations of each GO samples were added in a 250 mL beaker and subjected to magnetic stirring at 200 rpm. A Mettler-Toledo FiveEasy pH meter was calibrated and used to measure pH changes. Nitrogen gas was bubbled through the stirring liquid at a constant rate. The beaker was sealed with a rubber septum, while holes were made for the pH meter, the gas tube, and an inlet/outlet tube for addition of base/acid and/or extraction for zeta potential measurements. To facilitate liquid extraction for zeta, it was not feasible to keep the beaker/container completely airtight, however this setup does allow CO_2 expulsion during titration, while keeping the environment free from unwanted contamination. 1 M potassium hydroxide (KOH, R&M Chemicals) was added to the solution by pipetting 50 μL each time, allowing the pH to stabilize before taking measurements and extracting 0.50 mL for zeta potential measurements. To better observe the regenerative ability of the GO-hydronium layer, two separate pH readings were recorded, once

after 10 seconds of pH stabilization, and another after 20 seconds. The pH reading is considered stable when after 10 or 20 consecutive seconds, the pH stays within ±0.01, respectively. For zeta potential measurements, 0.5 mL of each solution was pipetted into a DTS1070 folded capillary cell which was inserted into a Malvern-Panalytical zetasizer nanoZS. The cell was equilibrated for 30 seconds at 25 °C and 3 runs were taken, for 10 measurements each. The Smoluchowski equation was used to calculate the zeta potential.

2.3. Cement microstructural analysis, heat and strength tests

Portland Cement Composite (YTL Castle, CEM II/B-L 32.5N, certified MS EN 197-1:2014) was used in all final cement and concrete samples. Fine and coarse aggregates were locally sourced from the Negeri-Sembilan quarry (river sand) in Malaysia with fineness modulus of 2.35, bulk density of 1350 kg/m^3, and specific gravity 2.6). For BET, FTIR, XRD, and SEM analysis, hydrated cement samples (control included) with a w/c ratio of 0.43 and polycarboxylate superplasticizer (Sika Viscocrete 1250NT, liquid) amount of 0.9% (by weight of cement) were prepared at 3, 6, 12, 24, 72 and 672 (28 days) hours of hydration. All GOs were added at 0.04% amount (by weight of cement) to distilled water, followed by the superplasticizer. The resulting solution was sonicated for 5 minutes before adding to cement for hydration. To terminate the hydration process (at the designated hours) as quickly as possible, the samples were manually crushed and freeze-dried for 72 hours (Martin Christ, -11 °C at 0.01 mbar), after which they were grinded (Retsch ZM200 ultracentrifugal mill, 0.2 mm sieve) and placed in a desiccator with silica gel until time of testing. The PANalytical X'Pert pro XRD was used for analysing the respective samples, over a rotation of 10° to 80° with a step size of 0.02° and scan time of 0.15 seconds, using Cu anode with K-α1 setting at 1.54060. Profex-BGMN software was used to perform Rietveld Refinement on the XRD scan data. The monoclinic Mumme and triclinic Belov structures were used for alite quantification. The micrometrics ASAP 2020 surface area and porosity analyzer was used to conduct BET tests for 24 hour freeze-dried samples only.

In the absence of an air-calorimeter (for isothermal calorimetry of hydrating cement), two DS18B20 (Maxim Integrated, 0.5 °C sensitivity) water-proof temperature sensors were connected to Arduino UNO micro-controller. One sensor was submerged in the hydrating cement mix to record the temperature changes over an approximately 24 hour period, while the other was kept outside the sample to record ambient temperature, and measurements were taken at 30 second intervals. Briefly, the hydrating cement's w/c ratio was reduced to 0.35, and superplasticizer amount reduced to 0.3% by weight of cement. All GOs were added at 0.04% amount (by weight of cement) to distilled water, followed by the superplasticizer. The wet cement mix was manually stirred and kept in a plastic cup inside a 500 ml glass beaker, which was placed inside a larger 2 L glass beaker, surrounded by insulating fabric to retain heat and minimize ambient temperature changes. The increase in heat was calculated by simply subtracting the external sensor's temperature reading from the internal sensor, and converted to joules by $Q = m_1c_1\Delta T + m_2c_2\Delta T$, where the mass, m and specific heat capacities, c are of water and cement, respectively and T is the recorded change in internal - external temperature readings. The obtained graphs were smoothed using a central moving average (uniform, rectangular) of 300 points. As such, these reading are meant to illustrate a significant change in hydration heat between control and GO cements, but however data is not precise enough for quantifiable analysis, and is not used as such accordingly.

10 mm diameter x 5 mm height cylindrical cement samples were prepared for X-ray micro-computed tomography analysis. The w/c ratio was set at 0.35 with 0.04% addition of each GO separately. After 14 days of curing in a moist temperature controlled environment, these samples were subjected for microCT scans using the Scanco Medical µCT35 instrument (Energy/intensity at 70kVp, 114µA, 8W), with high resolution and voxel size of 10 µm. A 7 mm x 7 mm x 2.32 mm rectangular block was cropped from the scanned results to ignore anomalies on the surface of the cured samples. These scans were processed using Slicer software, and the pores were isolated using image thresholding of the scanned slices, ignoring any pores smaller than 50 voxels. 3D segments of each pore were constructed to obtain their volumes for pore analysis.

The concrete was prepared in a weight ratio of 0.0004 : 0.009 : 0.43 : 1 : 1.96 : 3.18 of GO : polycarboxylate superplasticizer: water : cement : fine aggregates : coarse aggregates, respectively. The mix design was based on the BRE design method [19] (for control), aimed for a target strength of 40 MPa with 20 mm slump. The high amount of polycarboxylate superplasticizer was required to ensure the target slump of XGO-concrete. No GO was included in control samples. 4 mg/mL aqueous GO suspensions were subjected to ultrasonication for 15 minutes, before pouring into the remaining water for concrete mix, followed by polycarboxylate superplasticizer addition. Meanwhile, the required amounts of cement and aggregates were weighed and dry mixed in a pan mixer. The GO+superplasticizer was mixed for a few seconds, then poured slowly into the dry mix while the mixer was switched on. Total wet mixing time was controlled to maximum 10 minutes for each sample, after which

the machine was switched off and the mix was allowed to set. After 10 minutes the mix was poured (in 3 batches) into a slump cone (305 mm height, 100 mm top diameter and 200 mm bottom diameter) and tamped 25 times with a metal rod for each poured batch, before lifting the cone and measuring slump. The final slump value was recorded when consecutive slump tests for each type did not vary by more than 1 mm: most sample mixes gave the same consecutive slump after 3 tests, with the XGO based concrete mixes took 4 slump measurements to show similar consecutive slump. The mix was then poured (in 3 batches) into three respective 100 mm cubes and one 100 x 100 x 500 prism moulds, and subjected to 10 second vibrations via vibrating table for each batch. Once the moulds were fully filled and vibrated, they were left to harden for 24 hours, after which they were demoulded and placed in a water pond (pH 11) and water cured for 28 days. The Universal unit testing machine was used to perform 3-point bending tensile tests on the prism and compressive strength test on the cubes, respectively. It should be noted that flexural and slump tests are imprecise due to their testing methods/equipment and low number of samples, however concrete tests were performed solely to show how microstructural analysis results from cement can be translated effectively to concrete.

3. Results

3.1. GO characterization

Analytical characterization tests were performed to verify the chemical compositions of HGO, OGO, and XGO. X-Ray Photoelectron Spectroscopy (XPS) analysis is used to distinguish between the different chemical bonds of each GO, and their C1s peaks are shown in Figure 1(a). As the bond peaks overlap, peak-fitting is used to separate the spectra, and the results can be seen in Figure 1(b). HGO and OGO show similar peaks in XPS, while XGO-concrete shows significantly fewer counts per second. OGO has higher peak counts than HGO, however HGO has a higher C-O peak than C-C, indicating more hydroxyl group formation. HGO also has more carbonyl (C=O) groups than OGO. Meanwhile, XGO shows two separate peaks for C(O)O, indicating high carboxyl formation. As carboxyl groups are formed at the edges of GO sheets, and based on the poor counts in XPS analysis, XGO seems to be structurally defective. To better gauge this structural integrity for all GOs, Raman spectroscopy was performed (see Figure 1(c)). The graphitic G peaks indicate intact, non-oxidized regions in the GO sheets, while the D peaks show 'defects', caused by sp^3 bonding of O to the C atoms of GO. Hence, the ratio of the intensity of these peaks is calculated as I_D/I_G, a measure of the intactness of the GO sheets. HGO shows the lowest I_D/I_G (0.86), indicating high structural integrity, followed by XGO (0.99) and OGO (1.07), respectively. However, this test is also inconclusive, as higher I_D/I_G of GO can indicate either high oxidation degree or more structural defects in the GO sheet. Furthermore, research has indicated XPS and Raman analysis can reduce surface functional groups of GO during the measurements itself, either via prolonged exposure to X-ray sources, or thermal annealing during sample preparation [20]. The samples were then analyzed using Fourier-transform Infrared (FTIR) spectroscopy to further estimate the presence of functional groups (see Figure 1(d)). The high hydroxyl and epoxide presence is obvious in HGO, shown by high IR absorption between 1000 - 1200 cm^{-1}, which is attributed to C-O and C-O-C bond stretching. High O-H presence can also be seen at 3250 cm^{-1} bending and 1620 cm^{-1} stretching dips, however O-H is also present in any residual hydronium surrounding the GO, hence C-O bond absorption is a better indication of hydroxyl and epoxide presence in HGO. High C-C bond absorption is also observed for HGO, indicating high structural integrity and verifying the Raman spectral analysis. Thus, HGO is concluded to have high hydroxyl (and epoxide) groups, followed by OGO and XGO, respectively.

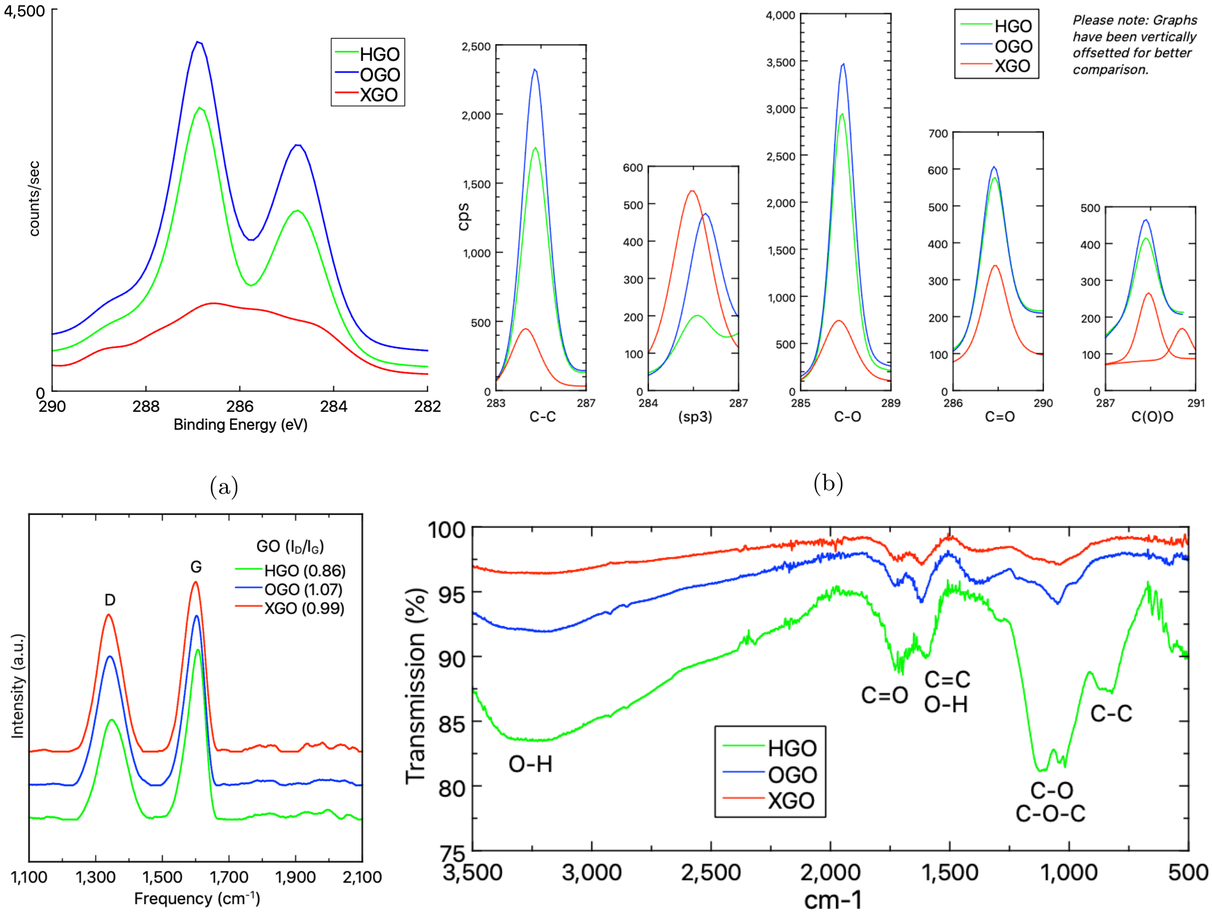

(a)

(b)

(c)

(d)

Figure 1: (a) The C1s XPS scan of HGO, OGO and XGO, with (b) isolated peak fittings for each bonds' respective binding energy. (c) Raman spectra with D and G peaks of GO samples, and (d) FTIR spectra of freeze-dried GO. Please note HGO, OGO, and XGO are vertically offset in each graph for clearer peak size comparison.

3.2. The hydronium activity of GO

The next step is to confirm whether high hydroxyl groups are producing a denser hydronium layer around the GO sheets. This layer is challenging to measure, as it exists in a dynamic equilibrium constantly reacting with the surface groups on GO [14]. Moreover, this layer can easily be destroyed by freeze-drying of GO. Hence, slow oven-dried and freeze-dried GO samples were tested to estimate the removal of hydronium, with the former is prepared by drying the GO without excessive hydronium removal. Electron Dispersive X-Ray (EDX) analysis of oven-dried GO samples show C/O ratios of 0.25 (for HGO), 1.42 (OGO), and 1.60 (XGO) (Supplemental Figure S1). HGO's ratio is not feasible, as there cannot be more than one O atom attached to a C atom in a GO sheet, or more than two O atoms attached to the C atom at the terminating edges of the GO sheet. Therefore, the excess oxygen count must be registering from the hydronium layer around HGO. FTIR analysis also shows significantly higher O-H absorption for the oven-dried HGO relative to freeze-dried

OGO (see Supplementary Figure S2), confirming HGO to have more surrounding hydronium than OGO or XGO, and this layer is removed freeze-drying. Atomic Force Microscopy (AFM) analysis is conducted to get visible confirmation of any surrounding hydronium, shown in Figure 2(a) and Supplementary figure S3. 3D profile of the AFM scans (see Figure 2(a)) highlight uniform bright spots on HGO's sheets reaching a height of 12 nm. OGO contains far fewer stacks reaching a height of 5 nm, followed by XGO having almost no bright spots at all. This is possibly the hydronium layer, though it may also be some oxidative debris. Furthermore, the structural defects created by XGO's thermal reduction are explicitly visible as holes and leaf-like shapes. Noteworthy, well dispersed, smaller GO sheets have shown to contribute higher available surface area for cement hydration, resulting in a denser and stronger cement structure [20. Thus, to account for the sheet sizes, Scanning Electron Microscopy (SEM) tests are performed on mica sheets spin coated with GO samples. HGO has the largest sheet with varied sizes (1.5 - 11 μm), followed by XGO (2 - 8 μm) and OGO (1 - 3 μm), respectively (see Supplementary Figure S4). SEM imaging shows visible evidence of stacked hydronium on HGO, which were removed upon freeze-drying, causing bulging and deformation of the GO sheets (Figure 2(b)).

3.2.1. Titration and zeta potential analysis

Based on the above tests, the hydronium layer is the largest in HGO, followed by OGO and XGO, respectively. Another way to quantify hydronium is by measuring the amount of base addition needed for complete pH neutralization of an aqueous GO solution. Hence, all GO samples were titrated, adding small amounts of 1M potassium hydroxide (KOH). However, GO's dynamic hydronium layer exists in an equilibrium state in water [14], so it follows that addition of base would disrupt this equilibrium, affecting the amount of GO hydroxyl deprotonation to create the hydronium layer. Assuming the change in equilibrium would take time to adjust, two sets of titration were performed for each GO sample. The first set recorded the pH value after each base addition once it stabilized for 10 consecutive seconds, while the second set recorded the pH value after 20 consecutive seconds of a stable reading. The reading is considered stable if the pH does not fluctuate by more than 0.01 for the time duration. HGO has a significantly bigger pH range between the two titration tests, followed by OGO and XGO, respectively (Figure 2(c)). This is remarkable: for instance, 0.005 mM base addition causes pH to rise to 9 (in the 10 second stability tests), but slowly gets neutralized back to pH 2.5 over 20 second stability readings. In addition, HGO's initial pH before any base addition is closer to 2, while OGO and XGO are approximately 3. This shows that HGO not only has a denser hydronium layer, but its layer can keep regenerating significant hydronium to neutralize the added hydroxides. OGO shows slightly higher pH resistance than XGO, and both show hydronium regeneration capabilities to a certain extent. Zeta potential tests are performed to study the net change in GO's surface charge as the base is added (Figure 2(d)), and HGO shows an unexpected increase (i.e. more positive) in net surface charge as the base is introduced, before decreasing to the expected -40 mV surface charge [22]. HGO also required more than twice the amount of $[OH]^{-1}$ to remove its hydronium layer completely.

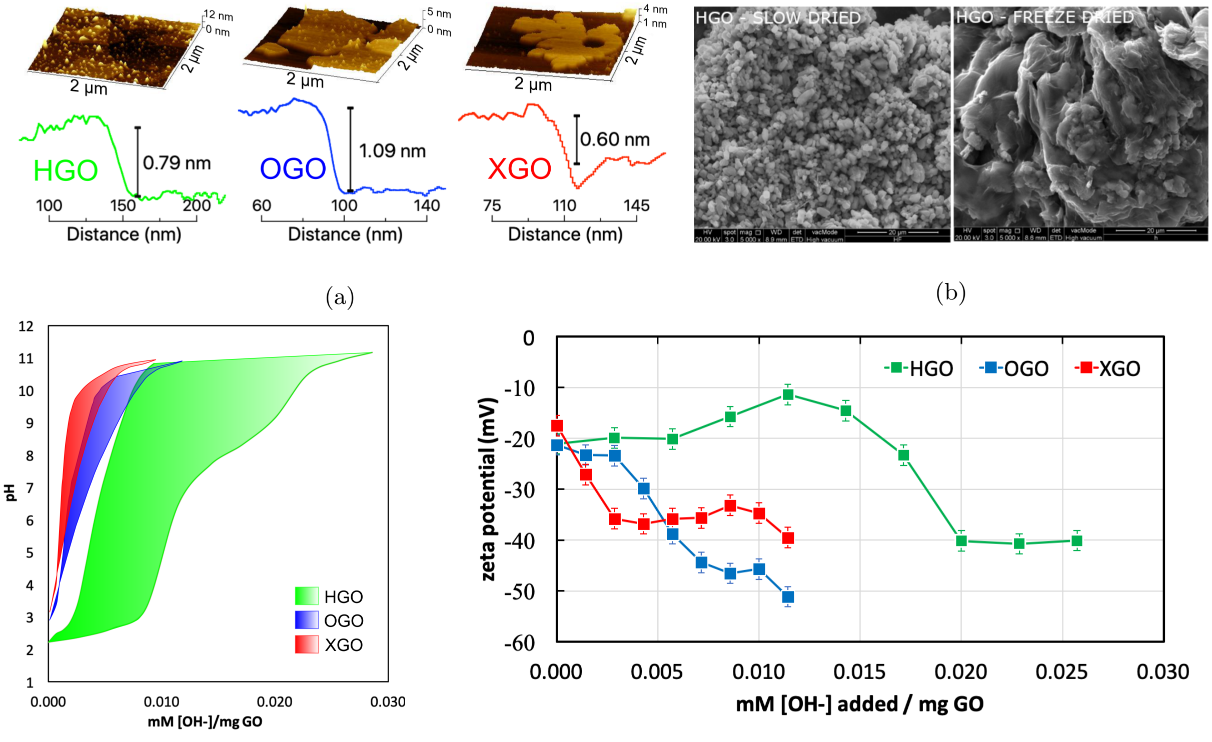

(a) (b)

(c) (d)

Figure 2: (a) The AFM 3D scan and thickness profile of HGO, OGO, and XGO. (b) SEM of HGO shows high water/hydronium stacking on oven dried HGO, and respective bulging deformation when freeze dried, (c) the pH ranges of all GO samples upon titration, and (d) surface charge increase showing hydronium regeneration for HGO, not prominent in OGO or XGO.

3.3. Illustration of hydronium activity on GO

To fully explain the significance of the titration and zeta potential results, the unique sheet structure of GO must be addressed first. The C atoms are typically connected to three other C atoms in the hexagonal graphene sheet structure. As carbon has 4 valence electrons, it can form a maximum of four covalent bonds, hence GO has O atoms grafted to these C atoms. As the H^+ interchange causes the build-up of hydronium layer, the deprotonated GO's hydroxyl groups can reform to epoxide groups, so long as a neighboring C atom has the available covalent bonding [13]. Conversely, epoxides open under presence of acid (such as hydronium) to form two separate hydroxyl groups. This illustrates how the dynamic hydronium layer may be affecting the types of functional groups on GO's surface. Furthermore, the hexagonal arrangement of C atoms in graphene allows valence electrons to freely travel between the atoms, resulting in an aromatic ring structure with high thermal and electrical conductivity. For GO, the oxidized zones hinder this electron transfer between oxidized and free C atoms, resulting in alternating C-C and C=C bonds through the oxidized sheets. These C=C bonds can shift through the structure, facilitated by the epoxide formations or openings, called vinylogous activity [14, 22, 23] (Figure 3(a)). It is believed that these bond changes are responsible for determining the equilibrium condition of the hydronium layer. HGO is more acidic than OGO or XGO, however these hydronium/GO interactions only allow some, but not all, of the GO hydroxyl groups to deprotonate. As such, it can be thought that HGO has a lot of *reserve* hydroxyl groups, that can deprotonate further should the equilibrium condition be shifted. This shift is introduced with base additions to the GO solutions, as the existing hydronium is reacting with hydroxide to form water molecules. The reduction in hydronium and the addition of new water molecules in GO's proximity cause a spike in the rate of deprotonation from the remaining GO hydroxyl groups, which is the shift in its dynamic equilibrium state. This explains why HGO not only resists a decrease in surface charge once base is added, but counters it (i.e. approaches 0) as recorded in the zeta potential tests. By comparison, OGO offers little resistance evidenced by the drop in surface charge, and XGO falls immediately as it has the least hydronium generation capability. This hydronium regeneration of HGO is only possible while hydroxyl groups remain protonated on GO (Figure 3(b)), and after a certain amount of $[OH]^{-1}$ is added, HGO fails to generate any more hydronium and its zeta potential falls to approximately -40 mV, typical of base-washed GOs [22]. It should be noted that zeta potential values can be off by ± 2 mV, due to the non-spherical shape and potential diffusion of ions through the hydronium layer on GO affecting accuracy of the tests [25].

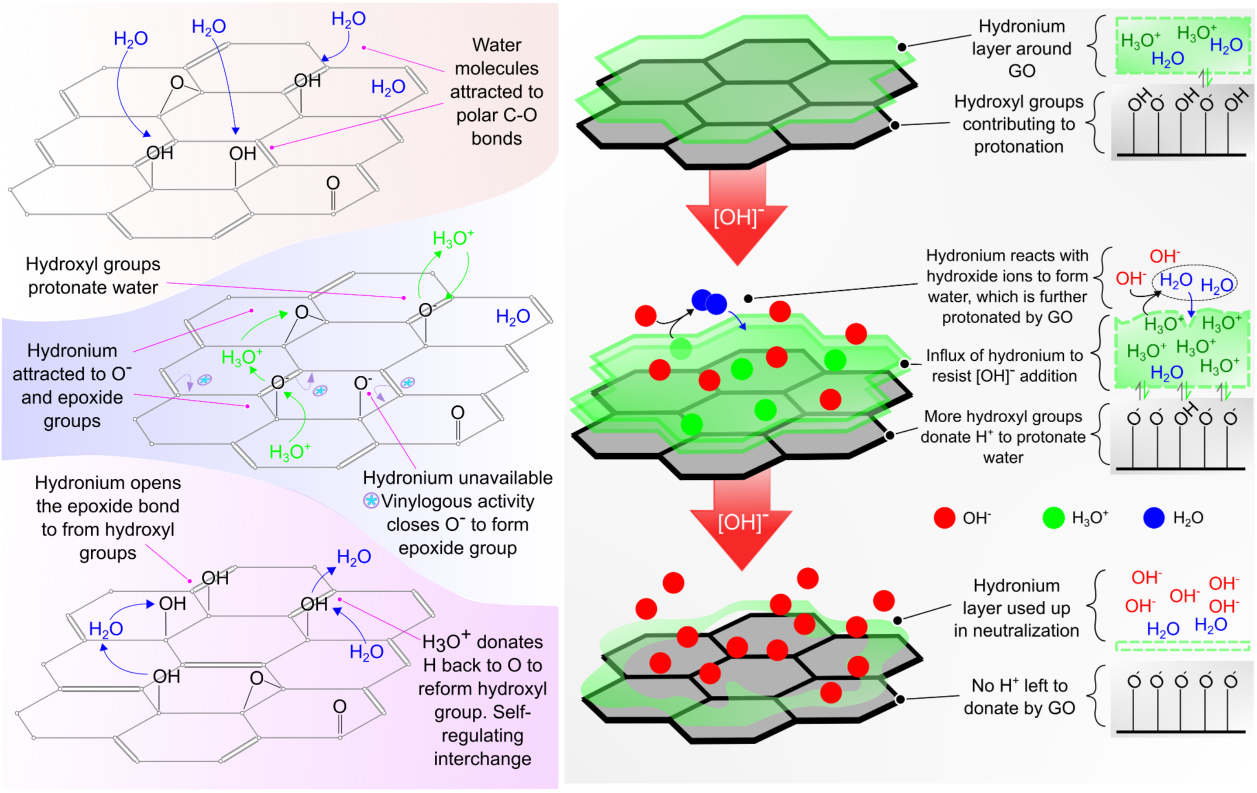

(a) (b)

Figure 3: Simplified models illustrating (a) the interchange of H^+ ions between GO and water, and (b) the regenerative hydronium ability of highly oxidized GO.

This regenerative ability of GO (specifically, HGO) is expected to play the primary role in the 'seeding' ability of GO during cement hydration. Calcium hydroxide ($Ca(OH)_2$) is a known by-product of PC hydration, and a known limiting factor in the mechanisms of cement hydration [26]. By neutralizing the $[OH]^{-1}$ produced during cement hydration, HGO-cement should optimize cement use and provide a stronger concrete structure, as discussed in the following section.

3.4. GO-cement performance

Unreacted water in the cement microstructure evaporates during its lifetime, leaving cracks and voids that leave the structure susceptible to chloride penetration and shrinkage. Hence, a finer microstructure is desirable as it prevents water from evaporating out of the structure.

3.4.1. Surface area analysis via BET tests

Brunauer, Emmett and Teller (BET) porosity tests indicate the average pore size for 24-hour hydrated control and GO-cements, during which the microstructure is fully developed, defining how strong the cement binding would be later in its life [26]. HGO-cement has $> 40\%$ single point surface area than control, followed by OGO-cement and XGO-cement, respectively (Figure 5(a)). Higher surface area leaves more open space for cement grains to hydrate in future, and indicates smaller pores in the sample, which was also confirmed by BET (average cement pore width with HGO = 18.2 nm, OGO = 22.6 nm, XGO = 24.5 nm, and control = 25.9 nm). Thus, HGO-cement has the densest microstructure at 24 hours of hydration, followed by OGO-cement, XGO-cement and control, respectively. The 12-hour hydrated cement samples are imaged via SEM, to observe how the microstructure is developed mid-hydration. All GO-cements have finer and more developed C-S-H growth than control, indicating cement dissociation and hydration has been accelerated (Figure 5(b)). Additionally, large $Ca(OH)_2$ crystals can only be seen in control samples. It is concluded that GO have somewhat neutralized the hydroxides, and minimized their crystal formations. The crystalline composition of the cement samples are needed to confirm this inference, hence X-Ray Diffraction (XRD) analysis is performed.

3.4.2. XRD and heat of hydration analysis

PC has various crystalline compounds, with some having multiple crystal phases, resulting in a highly complicated X-ray spectra from XRD tests. Rietveld Refinement is performed on the XRD data to determine cement's crystalline composition, by a semi-quantitative statistical peak fitting of XRD peaks. The XRD scans of all GO samples at various stages of hydration are showin in Figure 4. The consumption of alite is clearly evident in all samples from the diminishing of peaks at 32.5, 39, 41, 42, 52, 56.5, and 62.5 degrees, respectively. The vanishing of the 34° also signifies the usage of C_4AF in cement. However, due to the overlapping of peaks and the decrease in overall signal due to large peaks of calcite/limestone, Rietveld Refinement was performed to better ascertain the quantities of each compound in the sample, which is discussed in the main article.

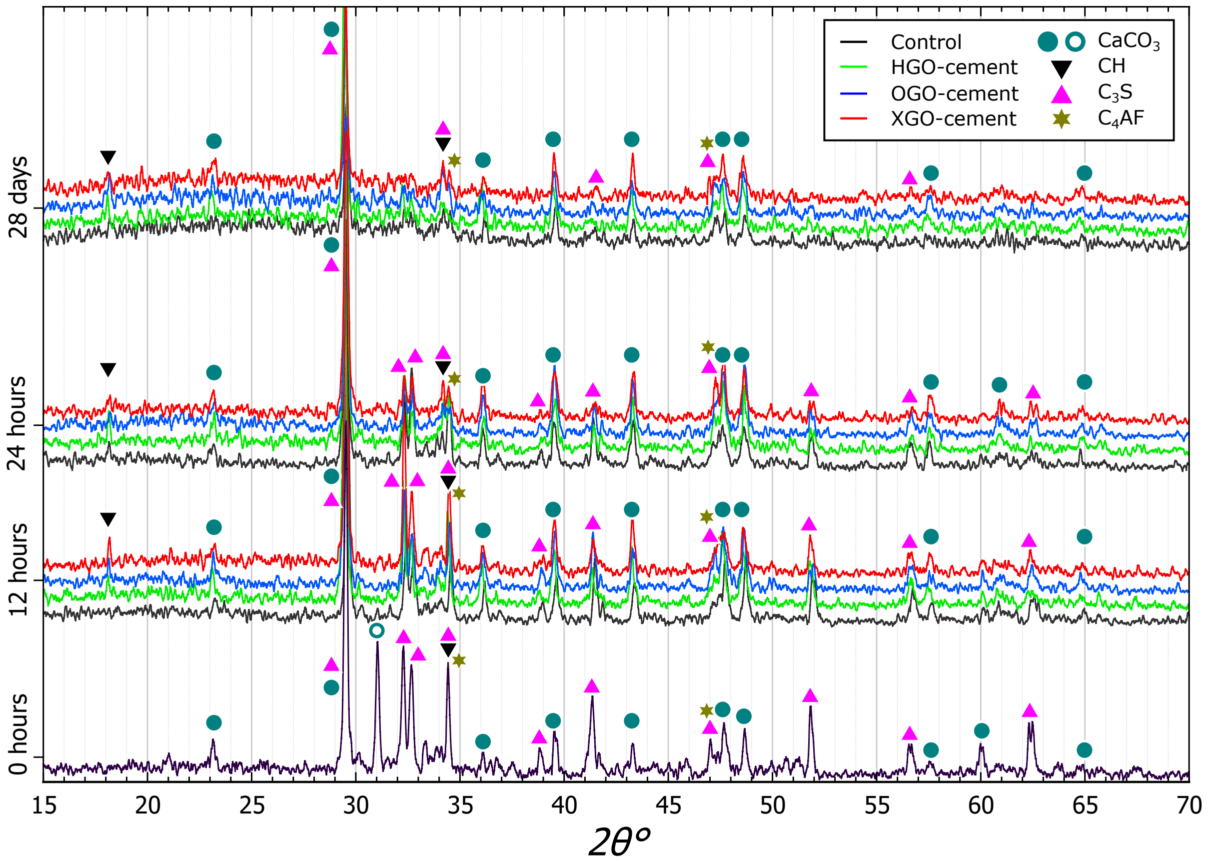

Figure 4: XRD scans of all cement samples from beginning of hydration (time = 0, cement), to 28 days.

C-S-H is difficult to measure in XRD due to it's amorphous, triclinic shape [27], but the cement hydration reaction uses alite ($3CaO.SiO_2$) and belite ($2CaO.SiO_2$) in cement to produce C-S-H ($3CaO.2SiO_2.3H_2O$), as outlined in these (approximate) equations:

$$6CaO.2SiO_2 + 6H_2O \rightarrow 3CaO.2SiO_2.3H_2O + 3Ca(OH)_2 \tag{1}$$

$$4CaO.2SiO_2 + 4H_2O \rightarrow 3CaO.2SiO_2.3H_2O + Ca(OH)_2 \tag{2}$$

Alite dissociates much faster than belite, and is the primary contributor to C-S-H during the first 28 days of hydration. Thus, Rietveld Refinement is used to find the amounts of alite and $Ca(OH)_2$ (portlandite) in control and GO-cements over 12 hours, 24 hours, and 28 days of hydration. At 12 hours, HGO-cement and OGO-cement show greater alite consumption than control, with XGO-cement the least (see Figure 3(c)). However, at 24 hours all GO-cements have alite at approximately 20%, far lower than control (at 34%). Over 28 days, XGO and OGO have used up even more alite, while HGO-cement's alite has stalled. Moreover, the amount of $Ca(OH)_2$ in 12 hour samples was highest in HGO, followed by both OGO and XGO, respectively, and least in control. This indicates all GO samples have accelerated hydration, as $Ca(OH)_2$ production and alite consumption is higher than control. Noteworthy, at 24 hours $Ca(OH)_2$ is highest in HGO, but these crystals appear lowest out of all samples at 28 days. This could be the neutralization of hydroxides due to HGO's hydronium layer. The crystallization of $Ca(OH)_2$ takes energy away from C-S-H growth [28, 29], therefore the hydroxide neutralization is an important factor that can propagate C-S-H growth over a longer time. Separately, higher $CaCO_3$ amounts were recorded in all GO-cement samples, a consequence of GO sheet destruction in alkaline environments, with the removed C atoms forming CO_2 in the cement samples (Supplementary Figure S5). The CO_2 can then react with CaO in the cement to form calcite ($CaCO_3$) [30]. This makes determining the exact alite consumption in GO-cements difficult, as some CaO is being diverted to calcite (not evident in control). Furthermore, SEM images did not show the presence of $Ca(OH)_2$ crystals in any GO-cements, despite the high XRD count. These crystals may be significantly smaller and harder to observe in the images, or their creation is localized in some GO-absent zones on the samples, not observed in our imaging process. To verify the hypothesis on increased GO-cement hydration, the heat released during the process was measured for the first 24 hours. Cement hydration is an exothermic reaction, and the change in released heat between the cements can enable us to confirm the XRD results. All GO-cement samples release greater heat in the first 24 hours relative to control, thus hydration has increased (Figure 5(d)). OGO and XGO's heat gain is also earlier than control, indicating the hydration reaction is accelerated, not evident for HGO. However, HGO released significantly more heat than OGO, XGO and control, respectively. Hence, it can be concluded that the hydronium layer is contributing to the increase in cement hydration. It should be noted certain aluminates in PC also contribute to the heat release, however the cement used in these experiments contains significantly lower aluminate amounts. Despite the increased and accelerated GO-cement hydration, they follow the same general heat curve of control cement, and XRD Rietveld Refinement analysis did not show any unique crystalline peaks, hence the GOs are acting as chemical catalysts for cement and not altering the cement matrix crystalline structure. The decrease in heat generated after 12 hours occurs due to total consumption of small alite particles, leaving only large crystals that do not dissociate completely [31], which cannot be affected by GO-incorporation to the authors' knowledge.

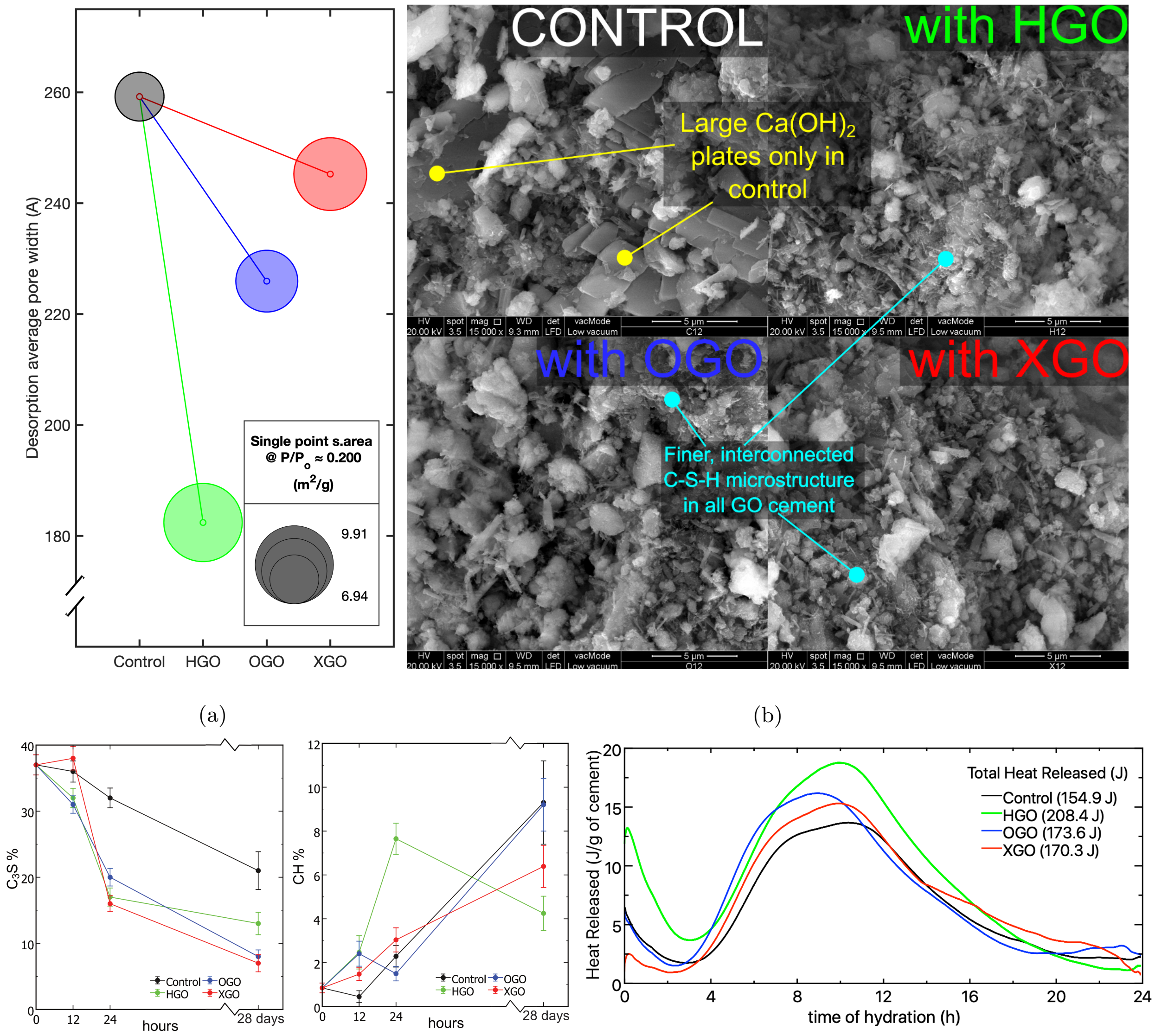

(a)

(b)

(c)

(d)

Figure 5: (a) The BET surface area and pore width (at 24 hours), (b) SEM (at 12 hours), (c) alite and Ca(OH)$_2$ content, and (d) heat of hydration (over 24 hours) of control, HGO, OGO and XGO cement samples.

3.4.3. Porosity analysis via MicroCT scans

MicroCT scans were performed on control and GO-cements to observe macro- and micro-pore formations, as opposed to nano-porosity analysis via BET. Figure 6(a) shows the isolated pore segments in each of the 7 x 7 x 2.32 mm cropped 14-day cement samples. Both HGO-cement and XGO-cement show noticeably less pore quantities with respect to control, and smaller pores in general. In contrast, OGO-cement possesses large pores similar to control, however the remaining pore sizes are quite small. A cumulative distribution of pore volumes show XGO-cement to have the highest number of pores, and the distribution is quite broad, signaling larger pores in the 0.005 mm^3 to 0.0005 mm^3 range (Figure 6(b)). It is followed by control, HGO-cement, and OGO-cement, respectively. OGO-cement (2066) and HGO-cement (2182) show significantly lower number of total pores compared to control (2634) and XGO-cement (2955), with similar slopes of the distribution curves. A comparable trend for all samples is seen for the equivalent pore size distribution (Figure 6(c)), where control shows the least smallest pore sizes, and XGO-cement shows the largest number of pores close to 40 μm size. Moreover, OGO-cement shows the least total number of pores, followed by HGO-cement. However, total pore volume is high for OGO-cement (2.55 mm^3), slightly larger than control (2.50 mm^3), and smaller for HGO-cement (1.78 mm^3) and XGO-cement (1.60 mm^3), respectively (Figure 6(d)). In summary, HGO-cement shows low total pore volume and less number of cumulative pores, further verifying its improved effects on the cement. Conversely, OGO-cement possessed the least total number of pores, but had considerably higher overall pore volume, owing to the existence of a few large sized pores evident in its segmentation 3D image. XGO-cement had highest number of pores, but lowest total pore volume, with larger number of 0.005 to 0.0005 mm^3 pores.

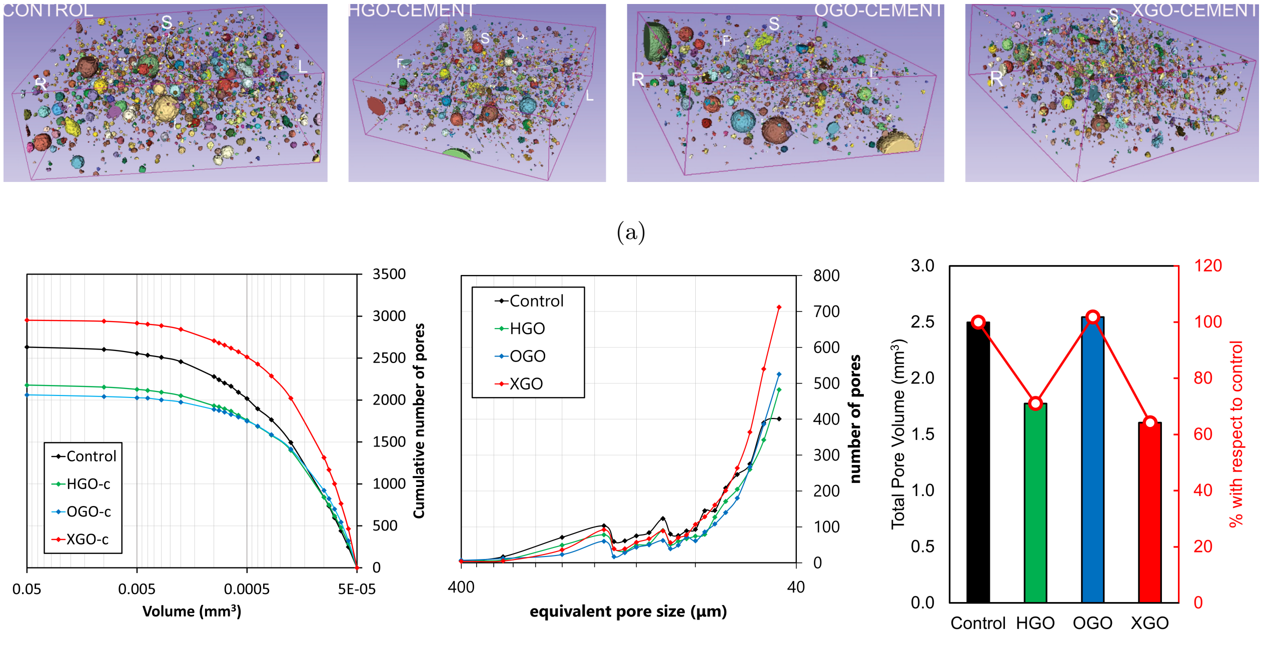

(a)

(b)

(c)

(d)

Figure 6: (a) 3D distribution of pores in all control and GO-cement samples. (b) Pore volume distribution for all CT scanned samples. (c) Equivalent pore diameter size for all CT scanned samples , and (e) Total pore volume and difference in %age between all samples, respectively.

3.5. Hypothetical model of early-age C-S-H/GO interactions

Based on the findings of the regenerative hydronium layer and GO-cement microstructure, molecular interactions between C-S-H and GO can be hypothesized. The growth of C-S-H on the GO sheet is simply highlighted in Figure 7(a). To further understand the Ca^{2+} inter-bridging, the C-S-H base unit is shown in

Figure 7(b). The Gartner et al.'s model [32] is applied here as it illustrates the hydrate layers in detail, which is important for outlining the role of hydronium with cement. Moreover, this highlights the importance of the intercalcium ions, which is the foundation for this research's hypothetical model [33]. The model consists of negatively charged calcium silicate oxide complexes, weakly held together by divalent Ca^{2+} ions in the hydrate layers, which also consist of OH^- and water molecules. The weak layer allows C-S-H to grow in different directions, making the dense cement matrix binding materials together. The hydrate layer is also the reason for C-S-H's amorphous (triclinic) crystal shape, making it difficult to detect via XRD tests [33]. The inner C-S-H layer is negatively charged due to the anionic Si-O-Ca-O-Si bridge, balanced by Ca^{2+}.

However, this may cause C-S-H to be electrostatically attracted to the positively charged, acidic hydronium. A plausible interaction scenario is shown in Figure 7(c). Once HGO comes in contact with a C-S-H bridge unit, OH^- ions from C-S-H's hydrate layer are neutralized by the hydronium ($H_3O^+ + OH^- \rightarrow 2H_2O$), and the resulting water molecules are used up by GO's hydroxyl group to regenerate the hydronium layer. Alternatively, the water can be used up for further alite dissolution resulting in more C-S-H, as outlined in Equation 1. Meanwhile, the floating hydronium could disrupt the C-S-H bridges by donating H^+ to the silicates, and as there is no divalent ion (Ca^{2+}) to hold the units together, they will drift away from one another. The drifting C-S-H units allow the binding material to grow longer and in all directions, away from the GO sheet until there is no hydronium in proximity. This explains the 'hairy' C-S-H growth on the HGO sheet, as shown in the SEM image in Graphical abstract. The inclusion of GO will also affect the 1 - 10 nm limits of nanoconfined water between the C-S-H layers [34]. Conversely, once the hydronium has been completely depleted in the alkaline environment, any remaining Ca^{2+} ions can bridge the deprotonated GO hydroxyl groups with the anionic C-S-H bridge units. That is the more likely scenario for XGO, where there is no regenerating hydronium to allow C-S-H drifting and expanding. The Ca^{2+} bonds C-S-H to the GO sheet, and also limits C-S-H to grow perpendicularly from the GO sheet (see Figure 7(d)). However, due to the limited direction of growth, C-S-H on GO may be dense but not as 'hairy', as there is no hydronium to generate water molecules to feed the C-S-H nucleation process. This is evident in the Graphical abstract, where XGO sheets have thin and dense C-S-H coatings. However, it should be noted that the removal of hydroxyl groups in synthesis of XGO results in lower dispersive ability than HGO, which explains the stacking of sheets in the image. Typically, C-S-H growth on GO should improve the flexural ability of the cement matrix, as the GO is now acting as physical reinforcement. However, this is only true if (i) the GO is successfully embedded in the hardened cement matrix, and (ii) the GO sheets themselves are strong enough material to substantially contribute to the flexural strength of cement. Molecular simulations show exfoliation of functional GO groups during any pullout force in the cement matrix, and the resistance to pull-out of GO groups is incumbent on the basal hydroxyl groups [35, 36]. Kai et al. [36] further concluded this resistance may carryover to their ability in arresting crack propagation in the cement matrix, as pure graphene nanosheets (i.e. with no functional groups) failed to inhibit crack openings or propagations in their simulations. Additionally, Zhang et al. [37] simulated the penetration of water between the C-S-H layers, and noted that the carbonyl bond (Ca and COO^-) were the strongest and most stable, as the hydroxyl groups lose structural H-bonds during their interactions with the increased penetrated water.

As the C-S-H and hydronium interactions have been explained, the results from Figures 5 and 6 can be further assessed. The micro-pore analysis using CT scans show largest number of small pores by XGO-cement, with HGO-cement and OGO-cement having less overall number of pores. HGO-cement shows smallest total number of pores and less overall total pore volume out of all the samples. The nano pore size recorded by BET tests are smallest for HGO, then OGO, XGO and control respectively, possibly due to the increased C-S-H growth and drifting ability from the hydronium on GO. HGO's heat of hydration is also far higher than control and remaining GO samples, verifying higher C-S-H production from alite and water's reaction (Equation 1) due to the neutralization of hydroxides by the hydronium layer. The decrease in heat evolved after 12 hours is sometimes attributed to lack of available water, reducing C-S-H growth [31]. However, HGO's heat curve decreases at significantly slower rate than the others, and coupled with lowering $Ca(OH)_2$ amounts after 24 hours, confirms that hydronium neutralization is providing water for further cement hydration. A major discrepancy is HGO-cement's stalling of alite consumption after 24 hours, which cannot be due to lack of available water as the hydronium neutralization in HGO-cement continues up to 28 days at least. A more sensible reason would be complete consumption of small alite particles, which have hardened the cement matrix around HGO, thus inhibiting greater dissolution. Ultimately, this indicates HGO's effects on C-S-H are quicker and shorter lived than other GO samples.

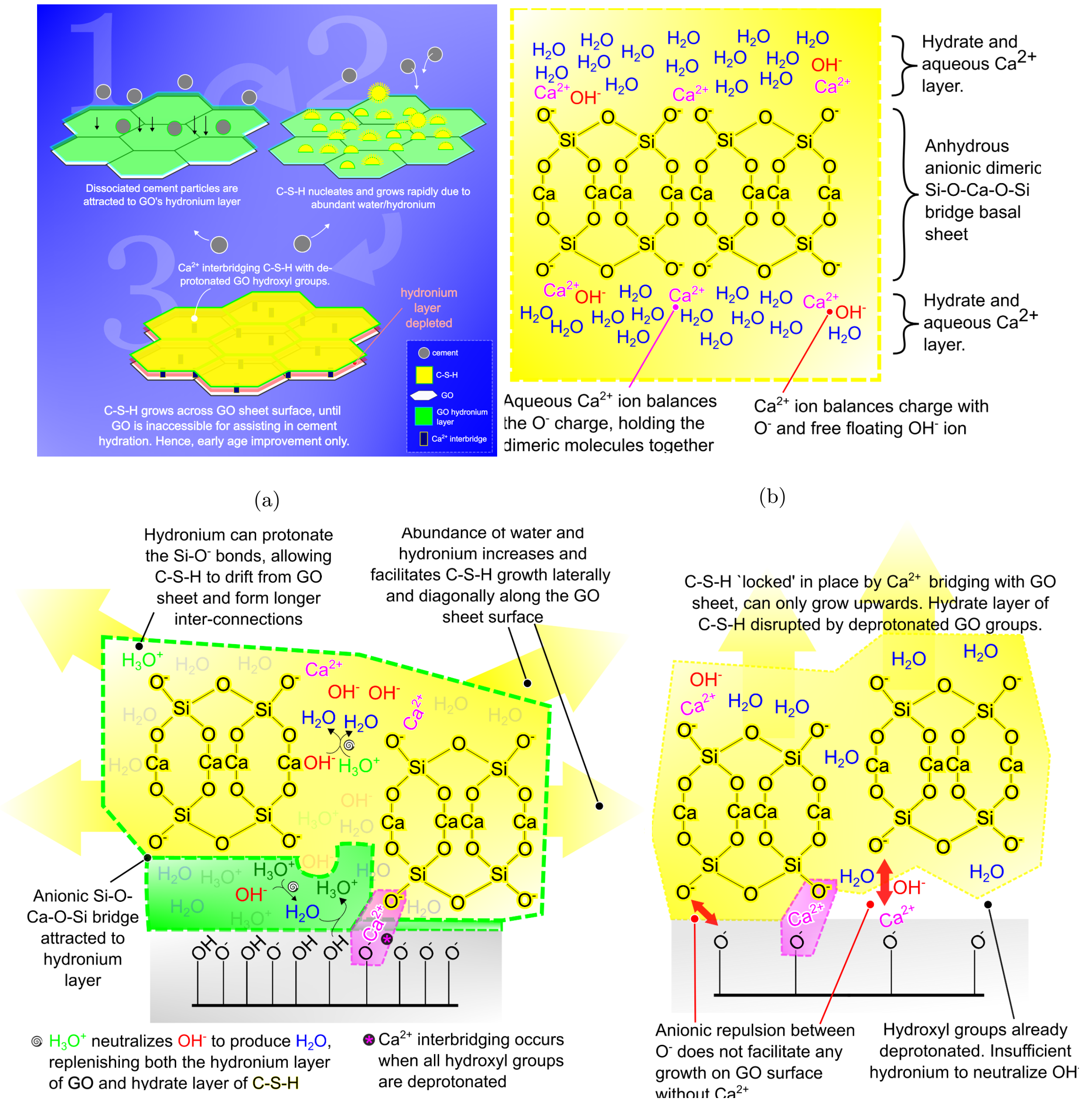

(a) (b) (c) (d)

Figure 7: Schematic diagrams of (a) how C-S-H grows on GO, (b) Gartner's C-S-H model unit, (c) how high-hydroxyl HGO regulates C-S-H growth and bridging, and (d) how low-hydroxyl XGO inhibits C-S-H growth and bridging.

3.5.1. Further study of hypothetical model via FTIR analysis

In research literature, molecular simulations of GO/C-S-H interactions show formation of 'cages', where the hydrate layer ions of C-S-H are locked between the GO sheet and C-S-H silicate units via Ca^{2+} interbridging [38]. One way to verify this is by FTIR analysis, which can detect the Si-O bond lengths in cement samples. If there is inter-bridging, the Si-O bond length will change, which will shift the absorption peak in FTIR spectra. Typically, the Si-O bond from C-S-H is registered at 970 cm^{-1} in FTIR analysis [39]. The shift in Si-O absorption peak over hours of hydration are shown in Figure 8(a) (and in Supplemental Figure S7), and there is an obvious rapid increase in the wavelength during the first 24 hours of hydration for all GO-cements. A higher peak wavelength implies reduced bond length, possibly due to the Ca^{2+} bridging of C-S-H silicate with GO sheets. The increase in wavelength is not uniform, however, possibly following the heat of hydration curve for HGO, OGO and XGO cements. Hence, based on the FTIR it can be postulated that there is Ca^{2+} inter-bridging, and furthermore the hydronium layer on GO is stopping these GO/C-S-H cage formations. It should be noted that while bridging GO and C-S-H possibly increases GO's ability to physically reinforce the cement matrix (by better bonding), it also reduces C-S-H's ability to grow and interconnect the entire cement microstructure. Moreover, keeping in mind the molecular simulations in literature [35-37, 40], the dense hydronium layer from HGO may cause an initial *decrease* in bond formations due to its location between the C-S-H and GO hydroxyl groups, but reactions with $Ca(OH)_2$ would rapidly neutralize, resulting in increased cement hydration and successful embedment of GO in the C-S-H layers. In FTIR, HGO-cement shows a smaller Si-O wavelength increase than OGO and XGO, respectively, due to its hydronium layer, however all GO-cements shift to a peak wavelength higher than 960 cm^{-1} at 28 days. For HGO-cement, this is due to complete depletion of the hydronium layer after being exposed to the alkaline environment, where most of the early-age hydration has already taken place by that period, thus the C-S-H growth was not hindered. As a confirmation, SEM images of 24-hour cement samples show smaller, more dispersed C-S-H in HGO-cement, where C-S-H is connecting the cement matrix together (see Figure 8(b)).

3.6. Effects of GO/hydronium-cement interactions on concrete

Finally, to show the strength contributions of all GO samples, 28-day compressive and flexural strength tests were performed on GO-concretes (Figures 8(c) and 8(d)). Compared to control, HGO-concrete is 30% stronger in compression, and 25% stronger in flexural strength, the strongest overall, followed by OGO-concrete and XGO-concrete, respectively. The flexural test shows less strength difference between the GO-concretes, which hints back to the physical reinforcement provided by GO as it is bonded in the cement matrix. XGO-concrete was only slightly stronger than control in flexural strength, despite its smaller GO sheet size (compared to HGO) which is supposed to improve the cement microstructure [21]. A possible answer for this is that XGO is structurally defective, as indicated by Raman (Figure 1(c)) and AFM (Figure 2(a)) analysis. Thus, it cannot provide strength improvement to concrete. There is a known compromise of using GO in cement, which is the reduction in workability (or flow) of the cement mix, attributed to accelerated cement hydration and the interbridging of GO sheets in the cement matrix [3]. Slump test was performed on the fresh mixes of all GO-concretes, and HGO shows almost 50% higher slump than control, a remarkable outcome (Figure 8(e)). By contrast, XGO shows a 40% lower slump than control mix. This further reinforces how hydronium initially prevents the C-S-H from coming into contact with, and hence being locked on, to the GO hydroxyl groups on sheet surface, via Ca^{2+} ions in C-S-H's hydrate layer. Of note, the smaller pores in XGO-cement observed from microCT analysis (Figure 6(a)) did indicate a denser microstructure, but it does not translate into concrete samples due to significant reduction in cement fluidity, resulting in sub-par strength of respective concrete. Conversely, the hydronium's interactions with C-S-H allow greater growth and drifting of particles that is attributed to the higher workability of HGO concrete (and OGO concrete) compared to control. This also indicates that highly oxidized GO can be used to optimize cement, leading to stronger and denser structures without compromising fluidity of the mix, a highly valued property of fresh mixes in the concrete industry. It may also reduce the need for additional superplasticizer consumption in concrete.

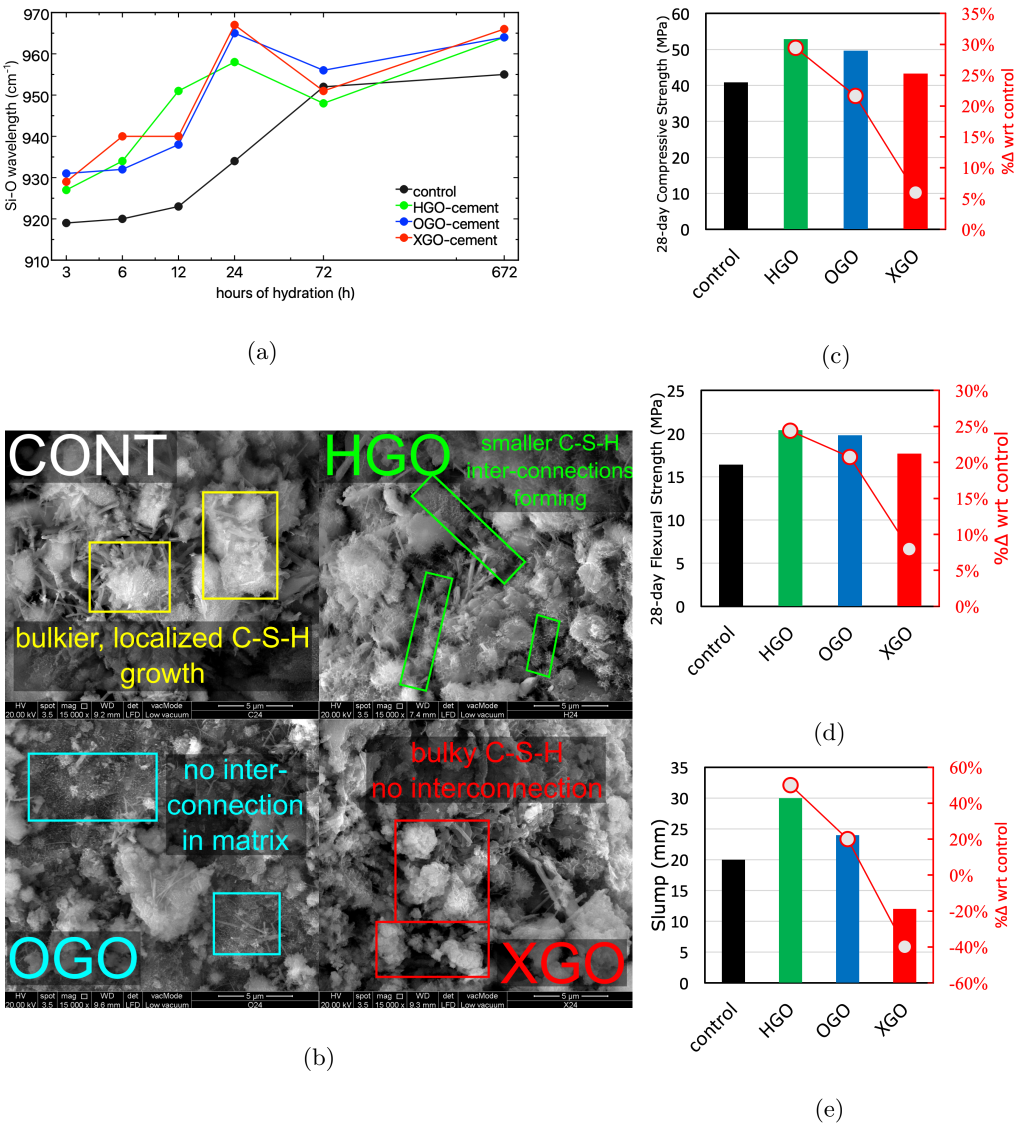

(a)

(c)

(d)

(b)

(e)

Figure 8: (a) The FTIR peak shifts of the C-S-H Si-O wavelength over hydration periods. (b) SEM images showing how HGO-cement's C-S-H is better dispersed in the cement matrix. (c) Bar graphs displaying the 28-day ultimate compressive strength, (d) 28-day ultimate flexural strength, and (e) slump test of fresh control, HGO, OGO, and XGO-concrete, respectively.

4. Conclusions

By modifying the synthesis of GO, 3 types of GO with varying hydroxyl groups were characterized to investigate GOs chemical interactions with hydrating cement. High-hydroxyl GO (HGO) formed a hydronium layer by donating protons in an aqueous solution. This hydronium layer is regenerating, as long as HGO has the ability to donate protons. As such, the layer is shown to be the first point of contact with hydrating cement, neutralizing hydroxides in the C-S-H layer and allowing C-S-H molecules to drift away from the GO sheet, improving interconnections in the cement matrix, resulting in a stronger, more durable cementitious structure with increased workability. It is important to include the hydronium layer in explaining GO-cement development, as the chemical interactions and workability differences of GO-cement and GO-concrete cannot be explained without taking it into account. Hence, it is believed the primary contributor to a stronger and denser hydrated cement is the hydronium generation (and regeneration) ability of GO, which is primarily dictated by its hydroxyl groups. This research presents a new use of the acidic capabilities of GO, showing significant enhancements in hydration, strength, workability and densification of cement by an easy, practical and economical GO application technique (*just add to water and mix with cement*).

However, there are several key interactions not covered in this research. Specifically, the reaction of GO with the aluminates in cement is not discussed, and late strength and durability of GO-cement also needs to be researched, taking into account the hydronium layer. Polycarboxylate superplasticizer was incorporated in cement and concrete samples to increase workability at low w/c ratios, however the chemical interactions between the superplasticizer and GO have not been investigated in great depth. The durability and corrosion resistance should logically also be improved due to the denser C-S-H microstructure, although GO's acidity may be detrimental to any steel in the structure, thus it remains to be tested. Lastly, it is imperative to define how long does GO remain acidic in an aqueous solution, with respect to its hydronium generating capabilities.

5. Conflicts of Interest

The authors declare no conflict of interests.

6. Acknowledgements

500 The main author acknowledges the University of Nottingham Malaysia for the PhD scholarship. Authors would also like to acknowledge the financial support from Ministry of Higher Education Malaysia via research grants FRGS/1/2019/STG05/UNIM/01/1 and FRGS/1/2016/STG07/UNIM/02/1.

References

[1] J. Lehne, F. Preston, Making Concrete Change Innovation in Low-carbon Cement and Concrete The Royal Institute of In-ternational Affairs, Chatham House Report Series, www.chathamhouse.org/sites/default/files/publications/research/2018-13-makingconcrete- c (2018) 138.
URL `www.chathamhouse.org`

[2] M. Rajczakowska, L. Nilsson, K. Habermehl-Cwirzen, H. Hedlund, A. Cwirzen, Does a high amount of unhydrated Portland cement ensure an effective autogenous self-healing of mortar?, Materials 12 (20) (2019). `doi:10.3390/ma12203298`.

[3] S. Chuah, Z. Pan, J. G. Sanjayan, C. M. Wang, W. H. Duan, Nano reinforced cement and concrete composites and new perspective from graphene oxide, Construction and Building Materials 73 (2014) 113–124. `doi:10.1016/j.conbuildmat.2014.09.040`.
URL `http://dx.doi.org/10.1016/j.conbuildmat.2014.09.040`

[4] S. Lv, S. Ting, J. Liu, Q. Zhou, Use of graphene oxide nanosheets to regulate the microstructure of hardened cement paste to increase its strength and toughness, CrystEngComm 16 (36) (2014) 8508. `doi:10.1039/C4CE00684D`.
URL `http://xlink.rsc.org/?DOI=C4CE00684D`

[5] L. Zhao, X. Guo, Y. Liu, Y. Zhao, Z. Chen, Y. Zhang, L. Guo, X. Shu, J. Liu, Hydration kinetics, pore structure, 3D network calcium silicate hydrate, and mechanical behavior of graphene oxide reinforced cement composites, Construction and Building Materials 190 (2018) 150–163. `doi:10.1016/j.conbuildmat.2018.09.105`.
URL `https://doi.org/10.1016/j.conbuildmat.2018.09.105`

[6] K. Chintalapudi, R. M. R. Pannem, The effects of Graphene Oxide addition on hydration process, crystal shapes, and microstructural transformation of Ordinary Portland Cement, Journal of Building Engineering 32 (May) (2020) 101551. `doi:10.1016/j.jobe.2020.101551`.
URL `https://doi.org/10.1016/j.jobe.2020.101551`

[7] I. Chowdhury, N. D. Mansukhani, L. M. Guiney, M. C. Hersam, D. Bouchard, Aggregation and Stability of Reduced Graphene Oxide: Complex Roles of Divalent Cations, pH, and Natural Organic Matter, Environmental Science and Technology 49 (18) (2015) 10886–10893. `doi:10.1021/acs.est.5b01866`.

[8] A. Peyvandi, P. Soroushian, A. M. Balachandra, K. Sobolev, Enhancement of the durability characteristics of concrete nanocomposite pipes with modified graphite nanoplatelets, Construction and Building Materials 47 (2013) 111–117. `doi:10.1016/j.conbuildmat.2013.05.002`.

[9] M. Wang, R. Wang, H. Yao, S. Farhan, S. Zheng, C. Du, Study on the three dimensional mechanism of graphene oxide nanosheets modified cement, Construction and Building Materials 126 (2016) 730–739. `doi:10.1016/j.conbuildmat.2016.09.092`.
URL `http://www.sciencedirect.com/science/article/pii/S0950061816315410?via{%}3Dihub`

[10] G. Jing, K. Xu, H. Feng, J. Wu, S. Wang, Q. Li, X. Cheng, Z. Ye, The non-uniform spatial dispersion of graphene oxide: A step forward to understand the inconsistent properties of cement composites, Construction and Building Materials 264 (2020) 120729. `doi:10.1016/j.conbuildmat.2020.120729`.
URL `https://doi.org/10.1016/j.conbuildmat.2020.120729`

[11] W. Gao, The chemistry of graphene oxide, Graphene Oxide: Reduction Recipes, Spectroscopy, and Applications (2015) 61–95`arXiv:arXiv:0811.1860v1`, `doi:10.1007/978-3-319-15500-5_3`.

[12] N. V. Medhekar, A. Ramasubramaniam, R. S. Ruoff, V. B. Shenoy, Hydrogen bond networks in graphene oxide composite paper: Structure and mechanical properties, ACS Nano 4 (4) (2010) 2300–2306. `doi:10.1021/nn901934u`.

[13] F. Mouhat, F. X. Coudert, M. L. Bocquet, Structure and chemistry of graphene oxide in liquid water from first principles, Nature Communications 11 (1) (2020) 1–9. `arXiv:1911.04987`, `doi:10.1038/s41467-020-15381-y`.
URL `http://dx.doi.org/10.1038/s41467-020-15381-y`

[14] A. M. Dimiev, L. B. Alemany, J. M. Tour, Graphene oxide. Origin of acidity, its instability in water, and a new dynamic structural model, ACS Nano 7 (1) (2013) 576–588. `doi:10.1021/nn3047378`.

[15] J. P. Rourke, P. A. Pandey, J. J. Moore, M. Bates, I. A. Kinloch, R. J. Young, N. R. Wilson, The Real Graphene Oxide Revealed: Stripping the Oxidative Debris from the Graphene-like Sheets, Angewandte Chemie 123 (14) (2011) 3231–3235. `doi:10.1002/ange.201007520`.

[16] X. Fan, W. Peng, Y. Li, X. Li, S. Wang, G. Zhang, F. Zhang, Deoxygenation of exfoliated graphite oxide under alkaline conditions: A green route to graphene preparation, Adv Mater 20(23) (2008) 4490-4493, doi: 10.1002/adma.200801306

[17] J. Chen, Y. Zhang, M. Zhang, B. Yao, Y. Li, L. Huang, C. Li, G. Shi, Water-enhanced oxidation of graphite to graphene oxide with controlled species of oxygenated groups, Chem. Sci. 7 (3) (2016) 1874–1881. `doi:10.1039/C5SC03828F`.
URL `http://xlink.rsc.org/?DOI=C5SC03828F`

[18] D. C. Marcano, D. V. Kosynkin, J. M. Berlin, A. Sinitskii, Z. Z. Sun, A. Slesarev, L. B. Alemany, W. Lu, J. M. Tour, Improved Synthesis of Graphene Oxide, ACS Nano 4 (8) (2010) 4806–4814. `arXiv:0410550`, `doi:10.1021/nn1006368`.

[19] D. C. Teychenné, R. E. Franklin, H. C. Erntroy, Design of normal concrete mixes, Building Research Establishment Ltd 331 (1) (1997) 46.
URL `https://epdf.pub/design-of-normal-concrete-mixes-br-331-ci-sfb.html`

[20] M. Rogala, P. Dabrowski, P. J. Kowalczyk, I. Wlasny, W. Kozlowski, A. Busiakiewicz, I. Karaduman, L. Lipinska, J. M. Baranowski, Z. Klusek, The observer effect in graphene oxide - How the standard measurements affect the chemical and electronic structure, Carbon 103 (2016) 235–241. `doi:10.1016/j.carbon.2016.03.015`.
URL `http://dx.doi.org/10.1016/j.carbon.2016.03.015`

[21] S. Sharma, N. C. Kothiyal, Influence of graphene oxide as dispersed phase in cement mortar matrix in defining the crystal patterns of cement hydrates and its effect on mechanical, microstructural and crystallization properties, RSC Adv. 5 (65) (2015) 52642–52657. `doi:10.1039/C5RA08078A`.
URL `http://xlink.rsc.org/?DOI=C5RA08078A`
URL `https://doi.org/10.1016/j.carbon.2020.01.022`

[22] T. Szabo, P. Maroni, I. Szilagyi, Size-dependent aggregation of graphene oxide, Carbon 160 (2020) 145–155. `doi:10.1016/j.carbon.2020.01.022`.

[22]

[23] A. L. Higginbotham, D. V. Kosynkin, A. Sinitskii, Z. Sun, J. M. Tour, Lower-defect graphene oxide nanoribbons from multiwalled carbon nanotubes, ACS Nano 4 (4) (2010) 2059–2069. `doi:10.1021/nn100118m`.

[24] P. D. Pancharatna, G. Jhaa, M. M. Balakrishnarajan, Nature of Interactions between Epoxides in Graphene Oxide, Journal of Physical Chemistry C 124 (2) (2020) 1695–1703. `doi:10.1021/acs.jpcc.9b10262`.

[25] G. V. Lowry, R. J. Hill, S. Harper, A. F. Rawle, C. O. Hendren, F. Klaessig, U. Nobbmann, P. Sayre, J. Rumble, Guidance to improve the scientific value of zeta-potential measurements in nanoEHS, Environmental Science: Nano 3 (5) (2016) 953–965. `doi:10.1039/c6en00136j`.

[26] J. W. Bullard, H. M. Jennings, R. A. Livingston, A. Nonat, G. W. Scherer, J. S. Schweitzer, K. L. Scrivener, J. J. Thomas, Mechanisms of cement hydration, Cement and Concrete Research 41 (12) (2011) 1208–1223. `doi:10.1016/j.cemconres.2010.09.011`.
URL `http://dx.doi.org/10.1016/j.cemconres.2010.09.011`

[27] J. W. Bullard, G. W. Scherer, An Ideal Solid Solution Model for C – S – H 4145 (2016) 4137–4145. `doi:10.1111/jace.14493`.

[28] I. Odler, H. Dörr, Early hydration of tricalcium silicate II. The induction period, Cement and Concrete Research 9 (3) (1979) 277–284. `doi:10.1016/0008-8846(79)90119-4`.
URL `https://linkinghub.elsevier.com/retrieve/pii/0008884679901194`

[29] P. W. Brown, C. L. Harner, E. J. Prosen, The effect of inorganic salts on tricalcium silicate hydration, Cement and Concrete Research 16 (1) (1986) 17–22. `doi:https://doi.org/10.1016/0008-8846(86)90063-3`.
URL `https://www.sciencedirect.com/science/article/pii/0008884686900633`

[30] S. A. Yaseen, G. A. Yiseen, Z. Li, Elucidation of Calcite Structure of Calcium Carbonate Formation Based on Hydrated Cement Mixed with Graphene Oxide and Reduced Graphene Oxide, ACS Omega 4 (6) (2019) 10160–10170. `doi:10.1021/acsomega.9b00042`.

[31] K. L. Scrivener, P. Juilland, P. J. Monteiro, Advances in understanding hydration of Portland cement, Cement and Concrete Research 78 (2015). `doi:10.1016/j.cemconres.2015.05.025`.

[32] E. Gartner, I. Maruyama, J. Chen, A new model for the C-S-H phase formed during the hydration of Portland cements, Cement and Concrete Research 97 (2017) 95–106. `doi:10.1016/j.cemconres.2017.03.001`.
URL `http://dx.doi.org/10.1016/j.cemconres.2017.03.001`

[33] E. Duque-redondo, P. A. Bonnaud, H. Manzano, Cement and Concrete Research A comprehensive review of C-S-H empirical and computational models , their applications , and practical aspects, Cement and Concrete Research 156 (April) (2022) 106784. `doi:10.1016/j.cemconres.2022.106784`.
URL `https://doi.org/10.1016/j.cemconres.2022.106784`

[34] P. A. Bonnaud, Q. Ji, K. J. Van Vliet, Effects of elevated temperature on the structure and properties of calcium–silicate–hydrate gels: the role of confined water, Soft Matter 9 (2013) 6418–6429. `doi:10.1039/C3SM50975C`.
URL `http://dx.doi.org/10.1039/C3SM50975C`

[35] M. Izadifar, J. S. Dolado, P. Thissen, A. Ayuela, Interactions between reduced graphene oxide with monomers of (calcium) silicate hydrates: A first-principles study, Nanomaterials 11 (9) (2021). `doi:10.3390/nano11092248`.
URL `https://www.mdpi.com/2079-4991/11/9/2248`

[36] M. F. Kai, L. W. Zhang, K. M. Liew, Graphene and graphene oxide in calcium silicate hydrates : Chemical reactions , mechanical behavior and interfacial sliding, Carbon 146 (2019) 181–193. `doi:10.1016/j.carbon.2019.01.097`.
URL `https://doi.org/10.1016/j.carbon.2019.01.097`

[36]

[37] T. Yang, Y. Jia, D. Hou, H. Li, J. Jiang, Molecular dynamics study on the weakening effect of moisture content on graphene oxide reinforced cement composite, Chemical Physics Letters 708 (August) (2018) 177–182. `doi:10.1016/j.cplett.2018.08.023`.
URL `https://doi.org/10.1016/j.cplett.2018.08.023`

[38] D. Hou, Z. Lu, X. Li, H. Ma, Z. Li, Reactive molecular dynamics and experimental study of graphene-cement composites: Structure, dynamics and reinforcement mechanisms, Carbon 115 (2017) 188–208. `doi:10.1016/j.carbon.2017.01.013`.
URL `http://dx.doi.org/10.1016/j.carbon.2017.01.013`

[39] R. Ylmén, U. Jäglid, B.-M. Steenari, I. Panas, Early hydration and setting of Portland cement monitored by IR, SEM and Vicat techniques, Cement and Concrete Research 39 (5) (2009) 433–439. `doi:https://doi.org/10.1016/j.cemconres.2009.01.017`.
URL `http://www.sciencedirect.com/science/article/pii/S0008884609000465`

[40] L. Lu, Y. Zhang, B. Yin, Structure evolution of the interface between graphene oxide-reinforced calcium silicate hydrate gel particles exposed to high temperature, Computational Materials Science 173 (November 2019) (2020) 109440. `doi:10.1016/j.commatsci.2019.109440`.
URL `https://doi.org/10.1016/j.commatsci.2019.109440`

Supplementary Material

Graphene oxide's regenerative acidity and it's effects on the hydration of Type II Portland Cement
Taimur Mazhar Sheikh, Mohammed Parvez Anwar, Kasturi Muthoosamy, Jayaprakash Jaganathan, Andy Chan, Abdullahi Ali Mohammed.

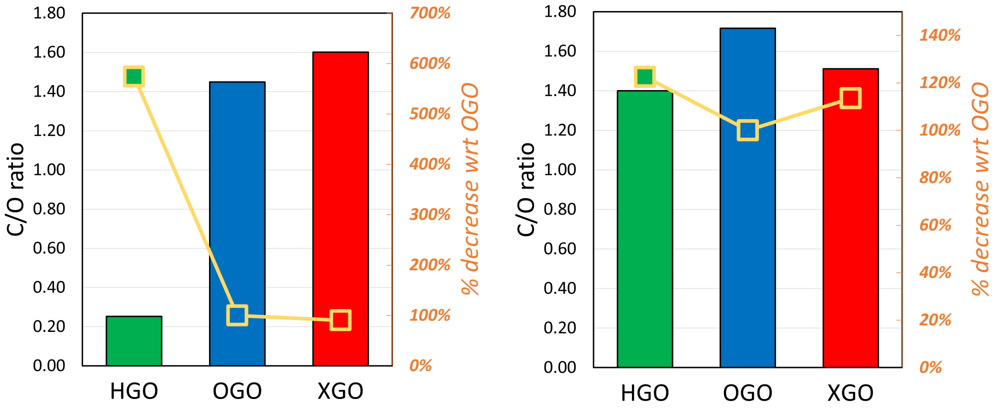

(a) (b)

Supplemental Material, Figure S1: Atomic C/O ratios obtained from (a) the EDX scan of oven-dried, and (b) EDX scan of freeze-dried HGO, OGO and XGO, respectively.

The secondary y-axis represents % decrease in oxidation ratio relative to OGO. As expected, oven-dried HGO shows the highest oxygen presence followed by OGO and XGO, respectively. This includes the hydronium layer coating on the GO sheet's surface. Upon freeze-drying the C/O ratios are similar, showing lowest oxygen presence for OGO, followed by XGO and HGO, respectively. The higher oxygen content for freeze-dried XGO may be due to its sheet defects leading to lower C-C and higher C=O presence.

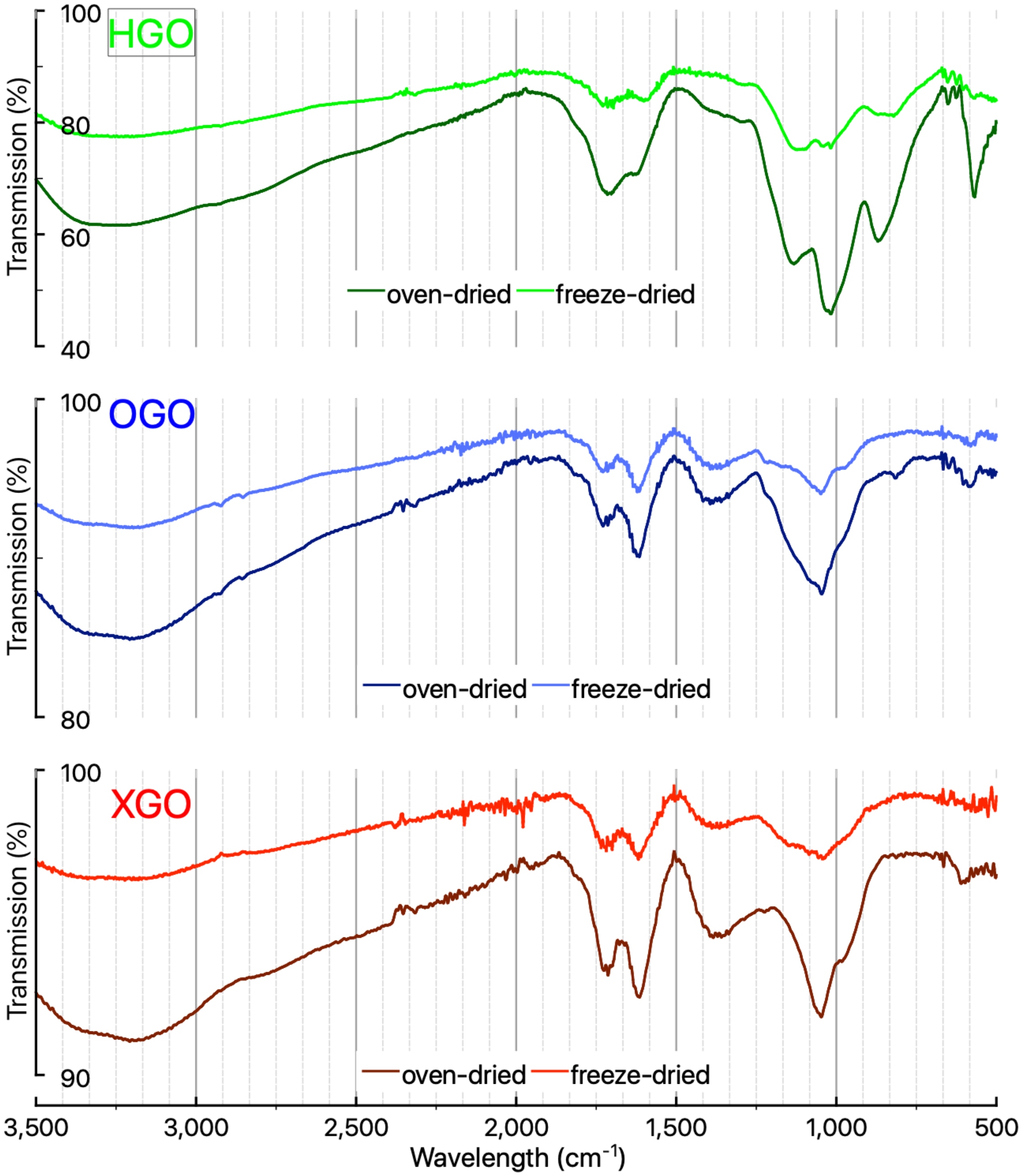

Supplemental Material, Figure S2: FTIR spectra of oven-dried and freeze-dried HGO, OGO, and XGO, respectively. For HGO, the 1020 cm^{-1} peak absorption is reduced relative to the other peaks. This may be due to forceful removal of C-O bonds during the freeze-drying process.

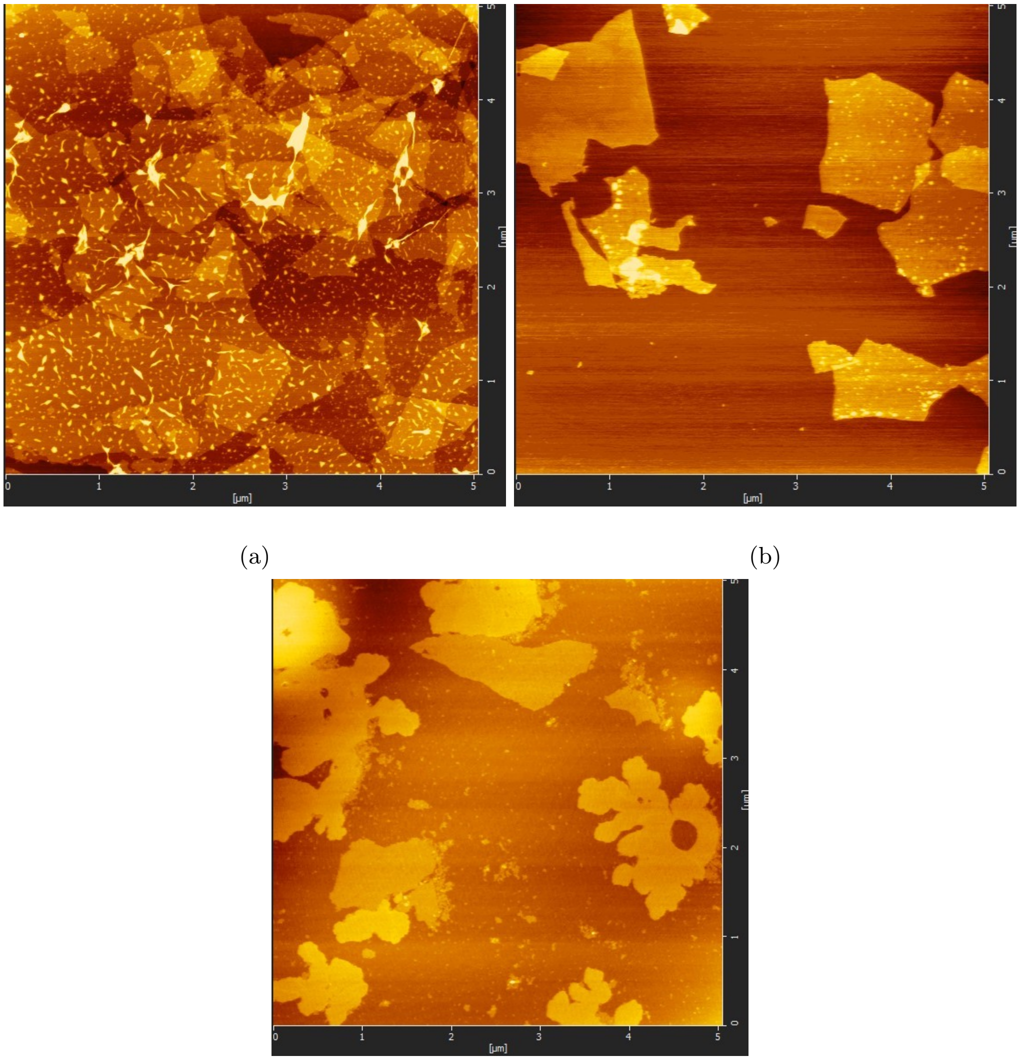

(a)

(b)

(c)

Supplemental Material, Figure S3: 5 μm x 5 μm AFM scans of (a) HGO, (b) OGO, and (c) XGO, respectively.

The high variance in HGO sheet size is clearly evident, as is the presence of hydronium as bright white spots in the scanned profile. OGO possesses fewer bright spots, least present in XGO. The structural defects in XGO due to its thermal reduction can also be observed.

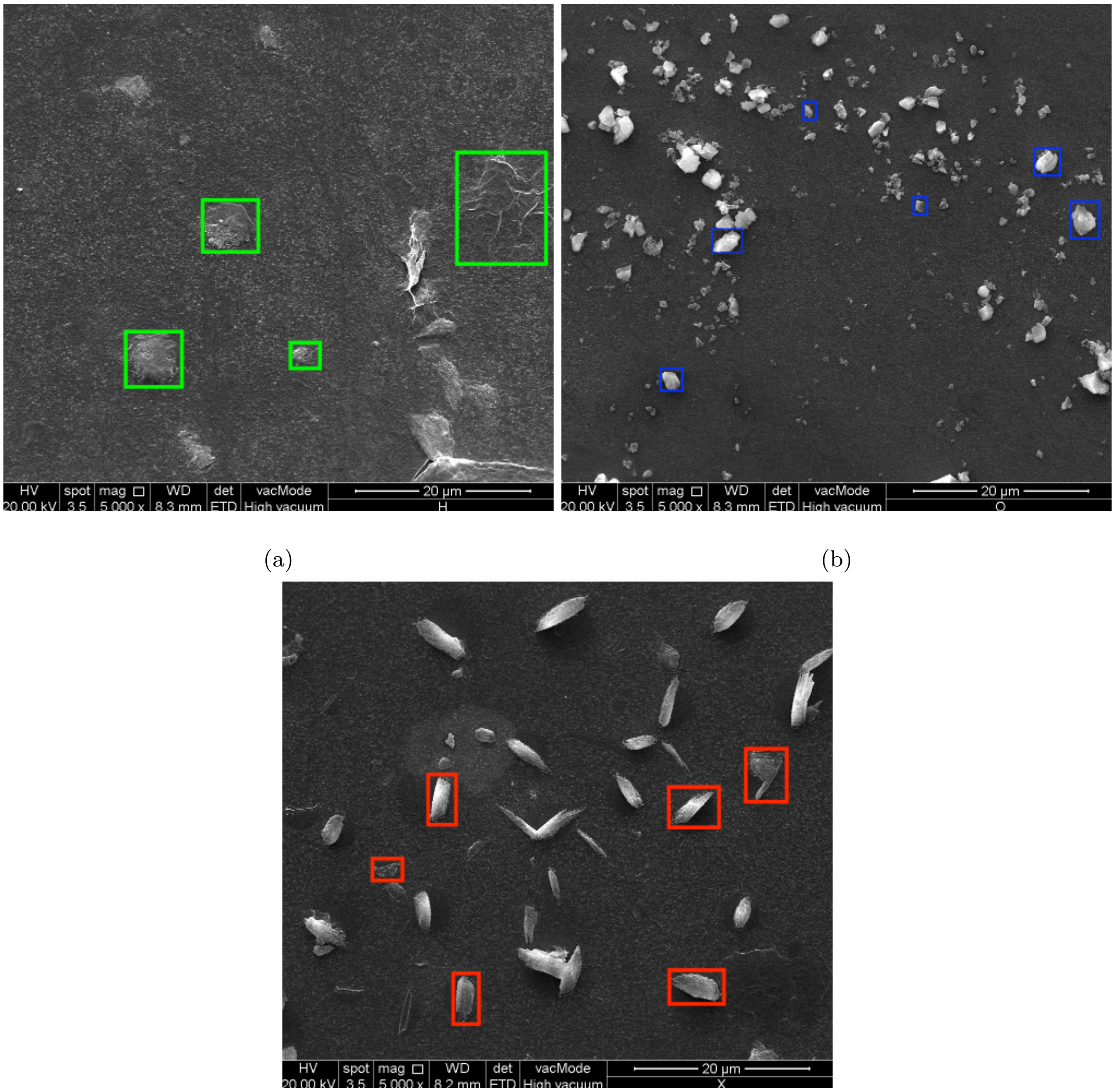

(a) (b)

(c)

Supplemental Material, Figure S4: SEM imaging of mica sheets spin-coated with (a) HGO, (b) OGO, and (c) XGO, respectively. Some of the sheets are highlighted in each image.

The sheet size ranges of all GO were obtained by SEM image thresholding and segmentation via MATLAB. Only the 20 largest measurements were kept. XGO shows higher stacking of sheets, presumably due to its poor dispersion upon thermal reduction. OGO shows very small sheets of consistent size.

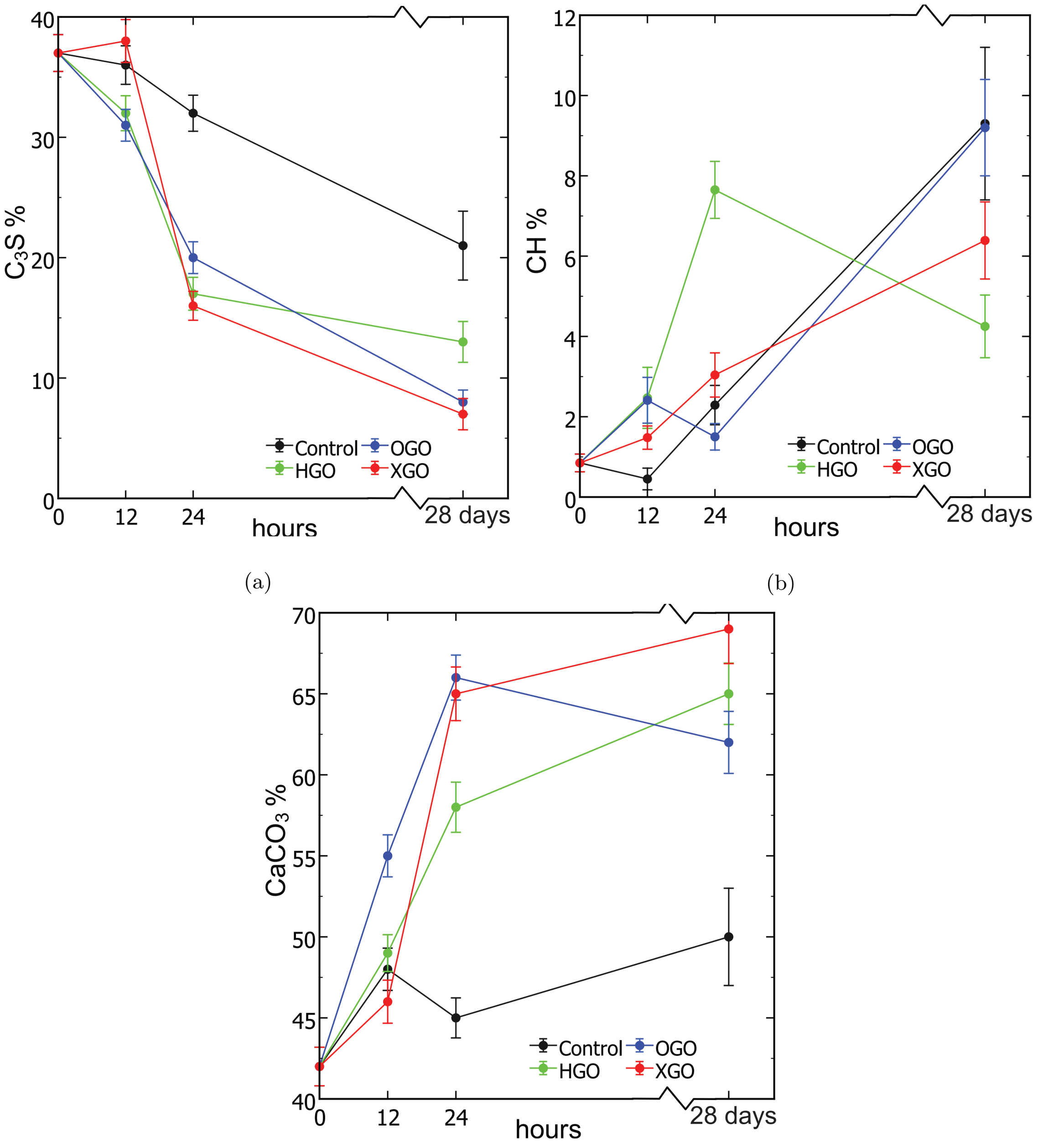

(a)

(b)

(c)

Supplemental Material, Figure S5: 12-hour, 24-hour and 28-day % amounts of (a) alite, (b) calcium hydroxide, and (c) calcite ($CaCO_3$) via XRD Rietveld Refinement analysis, respectively.

The high initial quantity of calcite is due to the use of the Type II PC with added limestone. The amount of calcite increased significantly in all GO-cements, but not in the control sample. As calcite is produced due to carbonation of CaO with dissolved CO_2 in the cement matrix, it is deduced that additional CO_2 is present in GO-cement, from the cleavage of C-C bonds in GO sheets, due to the alkaline environment. XGO, despite the low hydroxyl presence, is structurally defective due to its thermal reduction, and its further deterioration during cement hydration causes presence of high amounts of calcite. It is then followed by HGO, which may possess weak zones in the GO sheet due to high wrinkles from its additional functional groups (OH). The carbonation does not seem to directly hinder either the alite dissolution or calcium hydroxide production during cement hydration for all GO-cement samples.

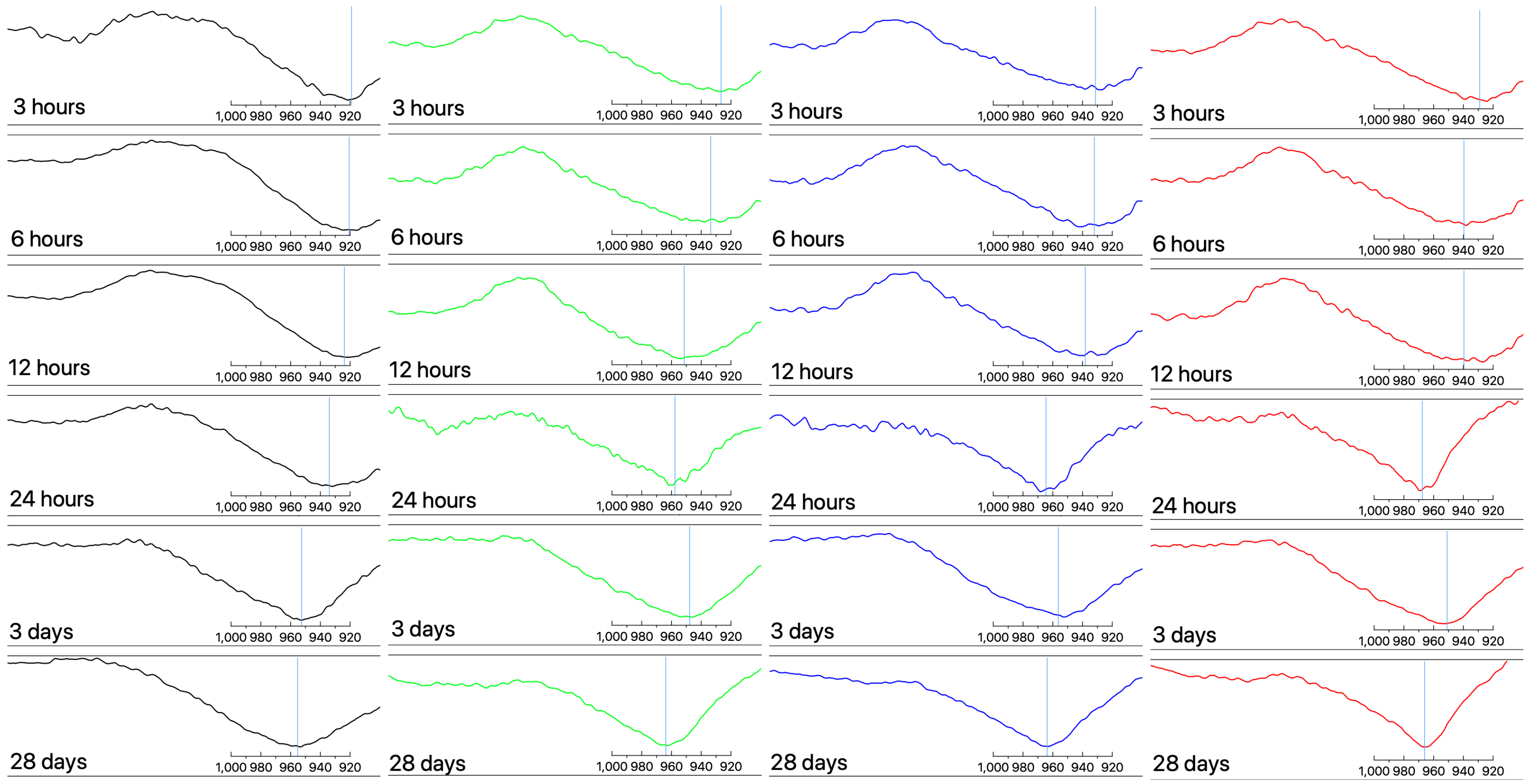

(a) (b) (c) (d)

Supplemental Material, Figure S6: Isolated silicate peak (Si-O) stretch from FTIR spectra of (a) control, (b) HGO-, (c) OGO-, and (d) XGO-cements over the 28-day hydration period, respectively.